PAPER

A Bayesian Complex-Valued Latent Variable Model Applied to FMRI

Chase J. Sakitis,[1] D. Andrew Brown[2] and Daniel B. Rowe[1,*]

[1]Mathematical and Statistical Sciences, Marquette University, 1313 W. Wisconsin Ave., 53233, WI, USA and [2]Mathematical and Statistical Sciences, Clemson University, 220 Pkwy Dr., 29634, SC, USA

*Corresponding author. daniel.rowe@marquette.edu

Abstract

In linear regression, the coefficients are simple to estimate using the least squares method with a known design matrix for the observed measurements. However, real-world applications may encounter complications such as an unknown design matrix and complex-valued parameters. The design matrix can be estimated from prior information, but can potentially cause an inverse problem when multiplying by the transpose as it is generally ill-conditioned. This can be combat by adding regularizers to the model, but does not always mitigate the issues. Here, we propose our Bayesian approach to a complex-valued latent variable linear model with an application to fMRI image reconstruction. The complex-valued linear model and our Bayesian model are evaluated through extensive simulations and applied to experimental fMRI data.

Key words: Bayesian, fMRI, reconstruction, regression, SENSE

1. Introduction

Background

Linear regression is a common tool used for prediction analysis of one variable based on the value of another variable. The equation for linear regression is that of a line of best-fit with measurement error as expressed in Eq. 1.1

$$y_j = \beta_0 + \beta_1 x_{j1} + \beta_2 x_{j2} + ... + \beta_p x_{jp} + \varepsilon_j, \quad j = 1, ..., n, \quad (1.1)$$

where p is the number of regression coefficients and n is the number of observations. Some applications, such as in fMRI image reconstruction, do not have a y-intercept in the model which would remove the β_0 from the model. For this paper, we will focus on the regression model with no y-intercept which can be compactly written as

$$y = X\beta + \varepsilon, \quad (1.2)$$

where $y \in \mathbb{R}^{n \times 1}$ is the observed dependent variable, $X \in \mathbb{R}^{n \times p}$ is the design matrix, $\beta \in \mathbb{R}^{p \times 1}$ is the vector of regression coefficients, and $\varepsilon \in \mathbb{R}^{n \times 1}$ is the measurement error or residuals. With regression models, our goal is to solve for the coefficients β. If the variables of this model are real-valued and the design matrix X is known, we can simply apply a least squares method to solve for β by using Eq. 1.3

$$\beta = (X'X)^{-1} X'y. \quad (1.3)$$

This linear model can encounter complex values instead of real-valued variables which changes y to $y_c \in \mathbb{C}^{n \times 1}$, X to $X_c \in \mathbb{C}^{n \times p}$, β to $\beta_c \in \mathbb{C}^{p \times 1}$, and ε to $\varepsilon_c \in \mathbb{C}^{n \times 1}$. With complex-valued parameters, we can write the linear model using a real-valued isomorphic representation to essentially remove the nuisance of complex values. This isomorphic representation is shown as

$$\begin{bmatrix} y_R \\ y_I \end{bmatrix} = \begin{bmatrix} X_R & -X_I \\ X_I & X_R \end{bmatrix} \begin{bmatrix} \beta_R \\ \beta_I \end{bmatrix} + \begin{bmatrix} \varepsilon_R \\ \varepsilon_I \end{bmatrix}, \ (\varepsilon_R, \varepsilon_I)' \sim N(0, \sigma^2 2 I_n), \quad (1.4)$$

where $y_R \in \mathbb{R}^{n \times 1}$ and $y_I \in \mathbb{R}^{n \times 1}$ are the observed real and imaginary components, respectively, of y, $X_R \in \mathbb{R}^{n \times p}$ and $X_I \in \mathbb{R}^{n \times p}$ are the unobserved real and imaginary components of X, $\beta_R \in \mathbb{R}^{p \times 1}$ and $\beta_I \in \mathbb{R}^{p \times 1}$ are the unobserved real and imaginary components of β, and $\varepsilon_R \in \mathbb{R}^{n \times 1}$ while $\varepsilon_I \in \mathbb{R}^{n \times 1}$ are the real and imaginary components of ε. This isomorphic representation can be compactly written to be $y = X\beta + \varepsilon$, where $y \in \mathbb{R}^{2n \times 1}$, $X \in \mathbb{R}^{2n \times 2p}$, $\beta \in \mathbb{R}^{2p \times 1}$, and $\varepsilon \in \mathbb{R}^{2n \times 1}$.

In real-world applications, we may not always have a known design matrix X. In this case, we may need to acquire other information to estimate our design matrix. This would allow us to treat the design matrix as "known," but is generally ill-conditioned leading to an inverse problem. To address this issue, a common solution is to add regularizers such as ridge (Hoerl and Kennard, 1970) or lasso regression (Tibshirani, 1996) to the model. These regularizers, however, may not always mitigate the problems as they can introduce bias which may lead to subjective parameter estimation or be computational expensive.

For this paper, we introduce a Bayesian approach to complex-valued latent variable linear model where the design

matrix X along with the regression coefficients β and the noise variance σ^2 are treated as unknown parameters. Prior distributions are then placed on the unknown variables and combined with the likelihood to get the joint posterior distribution. This model can be applied to any complex-valued data that can be modeled using linear regression.

An example of a complex-valued, latent variable real-world application can be seen in speech enhancement. For speech enhancement, the goal is to improve the quality of noisy signals (Loizou, 2013). Most models in speech enhancement ignore the phase information yielding real-valued signals (Williamson et al., 2013, 2014) that can be modeled using linear regression. Chen et al. (2018a) incorporates the phase information in the reconstruction of the complex-valued short-time Fourier transformation using a nonlinear complex-valued Gaussian process model. This work is further improved by adding in locality-preserving and discriminative constraints (Chen et al., 2018b). Despite the use of nonlinear models for the complex-valued speech signal data, linear regression can be used on the complex-valued signals (Schreier and Schraf, 2010). With available prior information (Williamson et al., 2013, 2014) and a complex-valued linear model, our Bayesian approach can be applied to speech signal data. Also, Nguyen et al. (2017) addresses the possibility of under-determined systems in the complex-valued linear regression, in signals such as speech, by using a generalization of sparse filtering and K-hyperlines clustering. Even with under-determined systems, our Bayesian approach can still be applied without any alterations creating a fully automated process.

Similar to signal processing, the data in functional magnetic resonance imaging (fMRI) is also complex-valued and can be modeled using a linear regression. To demonstrate the utilization of our proposed isomorphic Bayesian complex-valued latent variable model, we applied the model to simulated and experimental fMRI data for image reconstruction.

Overview

The second section of this paper will explain the model of the Bayesian complex-valued latent variable model. Section 3 of the paper describes the fMRI application with Section 4 analyzing the results of image reconstruction application. We will conclude in Section 5 with an overview of the important results of the paper and a discussion of future work.

2. Bayesian Complex-Valued Model

For our Bayesian model, we use the isomorphic representation of the complex linear model as expressed in Eq 1.4. In this work, two different representations of the design matrix will be used. The first representation is $X \in \mathbb{R}^{2n \times 2p}$ as shown in Eq. 1.4 is necessary for the proper skew symmetric design matrix for complex-valued multiplication. The second is $G = [X_R, X_I]$, used in the prior distribution and ultimately for parameter estimation, since X_R and X_I uniquely determine X and do not need to be duplicated.

Data Likelihood, Prior, and Posterior Distributions

We assume that the residual error is normal and independent and identically distributed in the real and imaginary components. The likelihood for the observed measurements for the n observations becomes

$$P(y|X, \beta, \sigma^2) \propto (\sigma^2)^{-\frac{2n}{2}} \exp\left[-\frac{1}{2\sigma^2}(y - X\beta)'(y - X\beta)\right]. \quad (2.1)$$

We can quantify available prior information about the regression coefficients β, the unobserved parameters of the design matrix X, and the residual variance σ^2 in the likelihood with assessed hyperparameters of prior distributions. The regression coefficients β are specified to have a normal prior distribution, expressed in Eq. 2.2. The design matrix, represented as G, is also specified to have a normal prior distribution (Eq. 2.3) and the noise variance σ^2 is specified to have an inverse gamma prior distribution (Eq. 2.4),

$$P(\beta|n_\beta, \beta_0, \sigma^2) \propto (\sigma^2)^{-\frac{2p}{2}} \exp\left[-\frac{n_\beta}{2\sigma^2}(\beta - \beta_0)'(\beta - \beta_0)\right], \quad (2.2)$$

$$P(G|n_X, G_0, \sigma^2) \propto (\sigma^2)^{-\frac{2np}{2}} \exp\left[-\frac{n_X}{2\sigma^2}tr(G - G_0)'(G - G_0)\right], \quad (2.3)$$

$$P(\sigma^2|\alpha, \delta) \propto (\sigma^2)^{-(\alpha+1)} \exp\left[-\frac{\delta}{\sigma^2}\right], \quad (2.4)$$

where tr is the trace of the $(G - G_0)'(G - G_0)$ matrix. The hyperparameters n_X, G_0, n_β, β_0, α, and δ are assessed from available prior information, but can also be determined using a fully subjective approach. The joint posterior distribution of the regression coefficients β, the design matrix X, and the noise variance σ^2 is

$$P(G, \beta, \sigma^2|a) \propto P(y|X, \beta, \sigma^2)P(\beta|n_\beta, \beta_0, \sigma^2)$$
$$\cdot P(G|n_X, G_0, \sigma^2)P(\sigma^2|\alpha, \delta), \quad (2.5)$$

with the distributions specified from Equations 2.1, 2.2, 2.3, and 2.4.

Posterior Estimation

Using the posterior distribution in Eq. 2.5, two approaches are used to estimate the regression coefficients β, design matrix X, and residual variance σ^2. Maximum *a posteriori* (MAP) estimation using the Iterated Conditional Modes (ICM) optimization algorithm (Lindley and Smith, 1972; O'Hagan, 1994) to find the joint posterior mode, and marginal posterior mean (MPM) estimation via Markov chain Monte Carlo (MCMC) Gibbs sampling (Geman and Geman, 1984; Gelfand and Smith, 1990). Beginning with initial estimates of each parameter, ICM iterates over the parameters, calculating its posterior conditional mode until convergence at the joint posterior mode. The posterior conditional modes are

$$\hat{\beta} = (X'X + n_\beta I_{2p})^{-1}(X'y + n_\beta \beta_0), \quad (2.6)$$

$$\hat{G} = (B'B + n_X I_{2p})^{-1}(BY' + n_X G_0), \quad (2.7)$$

$$\hat{\sigma}^2 = \frac{\Theta}{2(2n + 2p + \alpha + 2np + 1)}, \quad (2.8)$$

where $\Theta = (y - X\beta)'(y - X\beta) + n_\beta(\beta - \beta_0)'(\beta - \beta_0) + \alpha\delta + n_X tr[(X - X_0)(X - X_0)']$, $Y = [y_R, y_I]$ and $B \in \mathbb{R}^{2p \times 2}$ is a skew symmetric matrix representation of the regression coefficients β as expressed by

$$B = \begin{bmatrix} \beta_R & \beta_I \\ -\beta_I & \beta_R \end{bmatrix}. \quad (2.9)$$

The full conditional distributions are given by

$$\beta|X, \sigma^2, y \sim N\{\hat{\beta}, \sigma^2(X'X + n_\beta I_p)\}, \quad (2.10)$$

$$G|\beta, \sigma^2, y \sim MN\{\hat{G}, \sigma^2(B'B + n_X I_{2p})\}, \quad (2.11)$$

$$\sigma^2|\beta, X, y \sim IG(\alpha_*, \delta_*), \quad (2.12)$$

where $\alpha_* = np + n + p + \alpha$ and $\delta_* = [(y - X\beta)'(y - X\beta) + n_\beta(\beta - \beta_0)'(\beta - \beta_0) + n_X tr((G - G_0)(G - G_0)') + 2\delta]/2$. This

process is completely objective providing a fully automated method without having to calculate a subjective penalty. Our Bayesian approach, however, is flexible enough to include subjective priors if desired. Because we are using available prior information, we expect the subsequent estimators to have smaller variance. To illustrate this, extensive realistic simulations are performed in Section 4.

3. FMRI Application

FMRI Background

Magnetic resonance imaging (MRI) is a type of medical imaging that creates images using magnetic fields. Functional (fMRI) was developed in the early 1990's as a technique to noninvasively observe the human brain in action without exogenous contrast agents (Bandettini et al., 1993). This procedure examines brain activity by detecting changes in the brain using the blood-oxygen-level dependent (BOLD) contrast (Ogawa et al., 1990). When a neuron fires, the BOLD contrast increases in the proximity of the neuron and is a correlate for neuronal firing. The firing of neurons is a proxy for brain activity and is of interest when examining the brain in action in fMRI analysis. Measurements for images are arrays of complex-valued spatial frequencies in so called k-space (Kumar, Welti, and Ernst, 1975). These k-space arrays are then reconstructed into images using an inverse Fourier transform (IFT) producing brain images. The reconstructed brain images are made up of complex-valued voxels which contain the signal intensity for each pixel in the image. The magnitude and phase of the complex-valued reconstructed images can be utilized for analysis (Rowe and Logan, 2004; Rowe, 2005), but generally only the magnitude is used (Bandettini et al., 1993).

In fMRI, obtaining hundreds of volume images is necessary to detect activation in the brain. This series of observations are of the same underlying volume image taken over time. Measuring full arrays of data for all slices required to form volume images takes a considerable amount of time due to the size a dataset is from a single fMRI experiment. For example, the experimental data used in this paper contain nine slices of 96×96 images with 510 time points yielding 41,472,000 complex-valued data points. Acquiring fully sampled k-space arrays where every value in the array is measured limits the temporal resolution of the reconstructed images which can diminish effectively capturing brain activity.

Historically, a single channel receiver coil has been utilized in fMRI to measure fully sampled k-space. The drawbacks of acquiring fully sampled k-space arrays directed fMRI research to increase the number of images acquired per unit of time. More recently, the focus of research has been to acquire more images per unit of time by measuring less data without losing the ability to form a full image. To accomplish this, multiple receiver coils are utilized in parallel to each measure spatial frequencies. This would require the multiple coil images, after using the IFT, to be combined into a single, composite brain image. In 1999, Pruessmann et al. introduced a parallel imaging technique called SENSitivity Encoding (SENSE) which operates on the images after IFT.

The SENSE method uses the linear regression, as expressed in Eq. 1.2, with complex-valued parameters and a fixed design matrix. A complex-valued least squares solution (Eq. 1.3) is used to estimate the unknown parameter, which would be the voxel values of the single, full brain image. This approach for

parameter estimation can be difficult because the complex-valued design matrix, generally, is ill-conditioned. This can cause aliasing artifacts, low image quality, and signal-to-noise ratio (SNR) degradation in the final reconstructed image, which has lead to variations of the traditional technique (King and Angelos, 2001; Liang et al., 2002; Lin et al., 2004; Ying, Xu, and Liang, 2004; Liu et al., 2009). These modified regularization models have deficiencies that hardly mitigate the limitations of the traditional maximum likelihood SENSE procedure. These variations cause trade-off between SNR and aliasing artifacts (King and Angelos, 2001) or can lead to a significant increase in computational expense (Lin et al., 2004; Ying et al., 2004; Liu et al., 2009) due to selection of the regularizer which can render these techniques ineffective in practice. We can apply a Bayesian approach to this complex-valued linear model with an unknown design matrix called Bayesian SENSE (BSENSE). Our Bayesian model will incorporate prior information, which is assessed with complete automation and minimal computation time (less than one second) and does not use a single *a priori* fixed complex-valued sensitivity matrix. Through the extensive simulation study and application to experimental data, the results yield increased SNR, no aliasing artifacts, and increased image quality with improved task detection results.

For the fMRI application, the notation for the observed measurements (y), the design matrix (X), and the regression coefficients (β) in the linear model become a, S, and v, respectively.

Research Problem

As mentioned in the previous subsection, fMRI historically utilized a single channel receiver coil as illustrated in Figure 1. With a single channel coil, the height of the receiver is taller than the size of the subject's head, shown in the three-dimensional depiction in Figure 1a. Both parts a and b of Figure 1 show the single coil receiver wraps completely around the subject's head starting from posterior to anterior and connects back at the posterior.
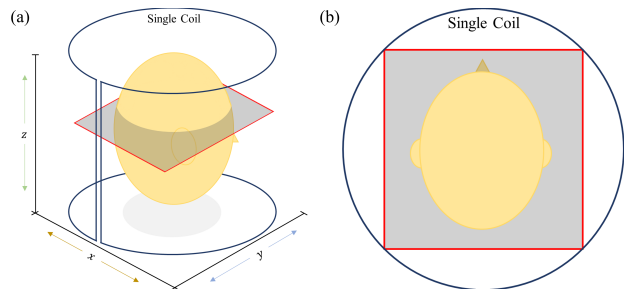

Fig. 1. (a) Illustration of a three-dimensional single coil channel along with (b) the top-down view of the coil receiver.

From the single channel coil, the k-space arrays are acquired along a trajectory as shown in Figure 2 (top left) where the machine starts in the bottom left corner and moves across the row measuring complex-valued spatial frequencies along the Cartesian grid. At the end of each row, you move up one line and the process is repeated in the opposite direction. This acquisition of complex-valued spatial frequencies is continued until all the rows of the k-space array is obtained, yielding fully sampled k-space depicted in Figure 2 (top right). These complex-valued spatial frequency arrays are then reconstructed

into full field-of-view (FOV) magnitude and phase brain images using the IFT (bottom of Figure 2). The reconstructed phase image is not shown.
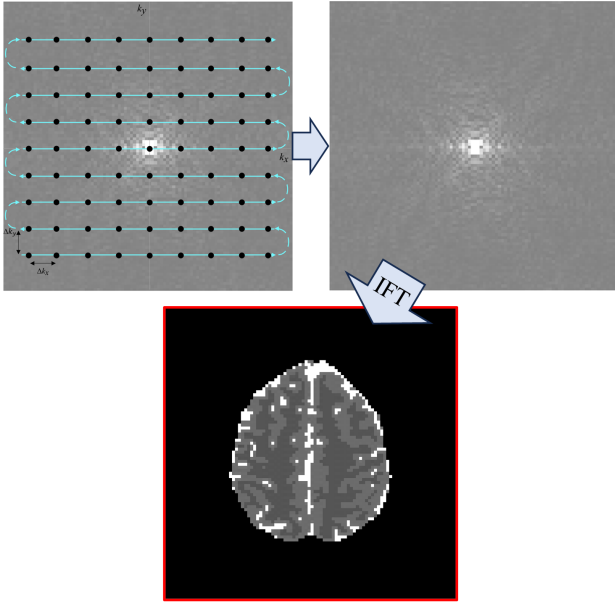

Fig. 2. Fully sampled k-space zig-zag coverage (top left) with the finalized full k-space array after omitting the turn-around points(top right) and the reconstructed brain image using the IFT (bottom).

To acquire more images per unit of time, $n_C > 1$ receiver coils are utilized instead of a single channel coil. The number of coils $n_C > 1$ would be the n observations as described in Subsection 1.1. An example of a four-channel coil arrangement is illustrated in Figure 3. The three-dimensional depiction of the multi-coil arrays in Figure 3a show the height of the receiver coils being taller than the head of the subject. In Figure 3b, starting with coil 1 at the anterior of the subject, the coils increment clockwise with coil 2 on the right lateral, coil 3 on the posterior, and coil 4 on the left lateral of the subject's head. Each of the four coils can measure full sampled k-space arrays, as exhibited in Figure 2, in parallel which does not increase the acquisition time compared to the single channel coil array.
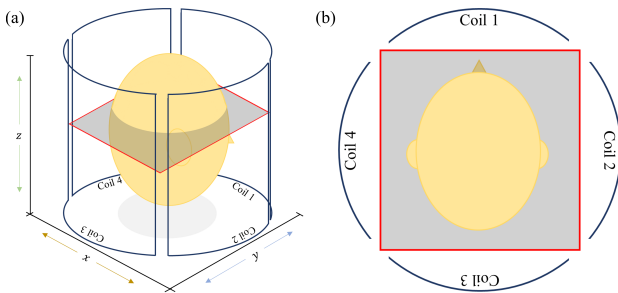

Fig. 3. (a) Illustration of a three-dimensional multi-coil channel with four receivers along with (b) the top-down view of the multiple coils.

Each channel receiver coil possesses a depth sensitivity profile which depends on its size and location. This means that each coil can only "see" parts of the object with a particular

depth sensitivity that decreases as we move farther from the coil. The same four-channel coil configuration in Figure 3b is displayed in Figure 4 (center image with four coils on each side) showing how the coils would look around a single slice brain image. Figure 4 gives an illustrative example of image slices with $n_C = 4$ coils (top, bottom, left, right) and their respective depth sensitivity to the true image slice (the four corners of the figure). The images for Figure 4 are magnitude images used to visualize the how the linear model is designed. In Figure 4, the top right corner image displays the true image point-wise multiplied by the depth sensitivity profile of coil 1 which is located at the front of brain. The resulting image shows that the signal intensity of the image decreases as you move farther from the coil location towards the back of the brain (bottom of the top right image). When examining a single complex-valued voxel in the weighted brain image for coil 1, the complex-valued voxel from the true image (center) is multiplied by the complex-valued weighted sensitivity, S_{1c}, to get $a_{1c} = S_{1c}v_c$. The other three coils follow this same operation creating the system of equations $a_c = S_c v_c$ where $a_c = [a_{1c}, a_{2c}, a_{3c}, a_{4c}]'$ and $S_c = [S_{1c}, S_{2c}, S_{3c}, S_{4c}]'$. With this system of equations, a_c is the complex-valued coil measurements (the observed measurements y from Eq. 1.2), S_c is the coil sensitivities (the design matrix X from Eq. 1.2), and v_c is the unaliased, and coil combined, voxel values (the regression coefficients β from Eq. 1.2). With this system of equations, a_c (the corner images in Figure 4) is the observed measurements, after applying the IFT, from the machine that need to be combined into a single, composite brain image. Since voxels are spatially discrete, this process is repeated for the rest of the voxels in the coil measurements.
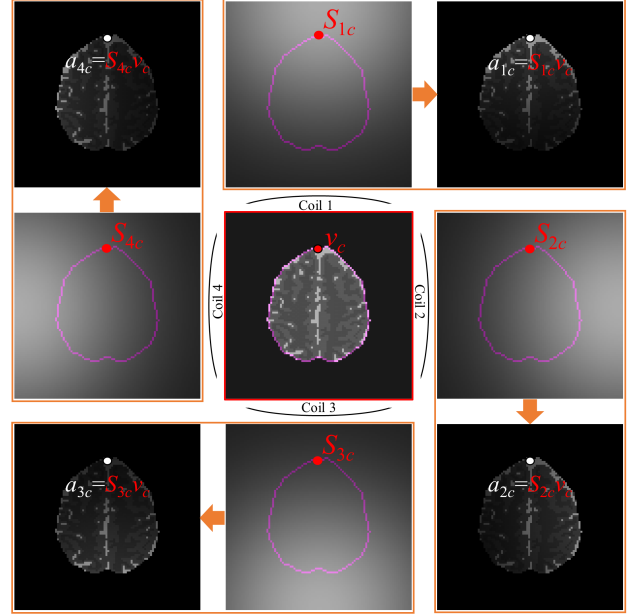

Fig. 4. True slice image (center) along with coil sensitivity profiles (top, bottom, left, right) and sensitivity weighted true images (the four corners). The coil sensitivity profiles are typically masked outside the brain but left here to show how the sensitivity decreases with voxels that are further from the coil.

As previously noted, the primary goal of parallel imaging is to increase the number of images acquired per unit of time which can be attained by measuring less data. This can
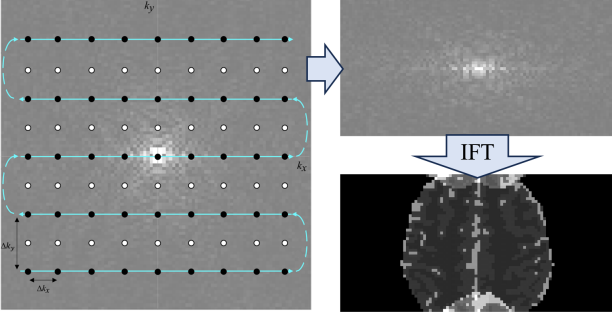
Fig. 5. Subsampled k-space zig-zag coverage with $n_a = 2$ acceleration factor (left), the finalized subsampled k-space array after omitting the turn-around points (top right) and the aliased brain image after reconstruction using the IFT (bottom right).
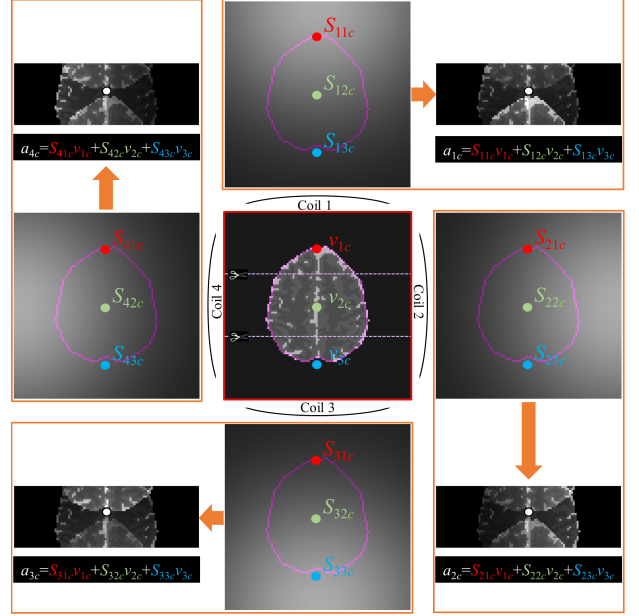

Fig. 6. True slice image (center) along with coil sensitivity profiles (top, bottom, left, right) and sensitivity weighted true aliased images (the four corners). The coil sensitivity profiles are typically masked outside the brain but left here to show how the sensitivity decreases with voxels that are further from the coil.

be accomplished by skipping lines in the k-space array, i.e. subsampling, as displayed in Figure 5. Skipping lines in k-space introduces what is called an acceleration factor, n_A. The acceleration factor indicates the fraction of lines of data in k-space that are measured and how much sampling time is reduced for a volume image. For example, with an acceleration factor of $n_A = 2$, every other line horizontally in k-space is measured as exhibited on the left side of Figure 5. This would result in each slice of the volume k-space arrays to be 48×96 (top right of Figure 5) instead of the full 96×96. If it took one second to obtain a full volume k-space array, with $n_A = 2$, the subsampled volume image would take half a second, doubling the rate at which we can observe brain dynamics. If an acceleration factor of $n_A = 3$ is used, a third of the points along the horizontal lines of k-space are measured yielding each slice of the volume image to be 32×96 which means three subsampled volume images would be observed in the time it would take to observe one full sampled volume image.

However, skipping lines in k-space causes reconstructed coil-weighted brain images to appear folded over itself, or aliased, because the IFT cannot uniquely map the downsampled signals. We can see an example of this in Figure 5 where the IFT of the subsampled k-space (top right), with $n_A = 2$, causes the brain image to be aliased (bottom right). The depiction in Figure 5 only shows the aliasing for one of the coils, and since multiple coils are utilized in parallel imaging, a weighted aliased image transpires for each coil. It also only shows the magnitude images as the associated phase images are not shown.

Figure 6 shows a similar depiction of the full coil-weighted magnitude brain images to Figure 4, but introduces an acceleration factor of $n_A = 3$. The sequential subsampling pattern follows one similar to that shown in Figure 5 (left), but measuring every third line of k-space instead of every other line, resulting in aliased coil-weighted brain images. In Figure 6 (top right), the true aliased image is the point-wise multiplication of the given voxel by the sensitivity profile for coil 1 summed for the three strips, $a_{1c} = S_{11c}v_{1c} + S_{12c}v_{2c} + S_{13c}v_{3c}$. This process is repeated for a_{2c} in coil 2 (bottom right), a_{3c} in coil 3 (bottom left), and a_{4c} in coil 4 (top left). This depiction of four observed, complex-valued aliased images, a_c, along with the unobserved, complex-valued coil sensitivities, S_c, the unobserved, complex-valued unaliased voxel values, v_c, and the complex-valued measurement error, ε_c, create a linear system of complex-valued equations, shown in Eq. 3.1. Since the unaliased voxel values, v_c, are the parameter of interest, SENSE estimates the coil

sensitivities, S_c, treats it as a known parameter, and models the process as a complex-valued regression model,

$$\begin{bmatrix} a_{1c} \\ a_{2c} \\ a_{3c} \\ a_{4c} \end{bmatrix} = \begin{bmatrix} S_{11c} & S_{12c} & S_{13c} \\ S_{21c} & S_{22c} & S_{23c} \\ S_{31c} & S_{32c} & S_{33c} \\ S_{41c} & S_{42c} & S_{43c} \end{bmatrix} \begin{bmatrix} v_{1c} \\ v_{2c} \\ v_{3c} \end{bmatrix} + \begin{bmatrix} \varepsilon_{1c} \\ \varepsilon_{2c} \\ \varepsilon_{3c} \\ \varepsilon_{4c} \end{bmatrix}. \quad (3.1)$$

BSENSE uses the isomorphic representation of Eq. 3.1, similar to Eq. 1.4 (Bruce et al., 2012). The likelihood, prior distributions, and posterior along with the parameter estimation are outlined in Section 2.

Hyperparameter Determination

The full pre-scan coil calibration images can be utilized to fully assess appropriate hyperparameters for the prior distributions in an automated way. For example, the n_{cal} coil calibration images (top left of Figure 7) can be averaged together to give us full complex-valued coil images. An initial magnitude v_{0M} of the prior mean can be estimated for each voxel in the unaliased image by computing the Euclidean norm shown in the top right of Figure 7.

The n_C averaged coil calibration images can then be pointwise divided by v_{0M} to obtain a prior mean for the real and imaginary coil sensitivities, as displayed in the bottom of Figure 7. The phase of the coil sensitivities is estimated by $arctan(I/R)/2$ where R and I are the real and imaginary components of the coil sensitivities, respectively. This phase is utilized to estimate complex-valued prior means for the coil sensitivities, H_0. These coil sensitivity estimates, H_0, along with the full averaged calibration coil images are used to estimate complex-valued prior means for the voxel values, v_0.

The hyperparameters n_S and n_v, which are the scalar weights of the prior means, are assessed to be the number of
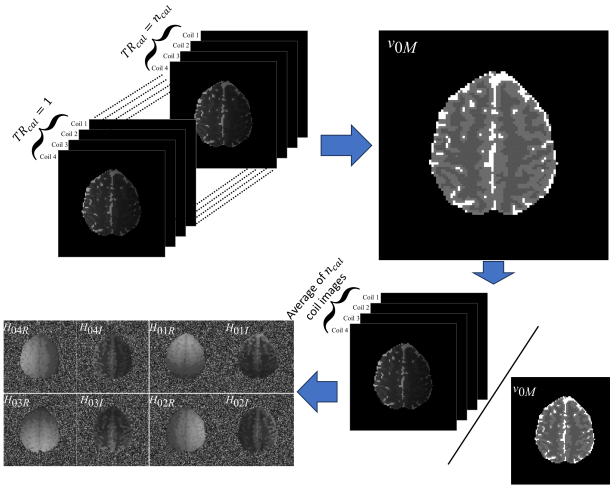
Fig. 7. The n_{cal} calibration coil images (top left) are averaged through time and the Euclidean norm is taken yielding a prior mean for the magnitude unaliased voxel values v_{0M} (top right). The average of the coil calibration images are then pointwise divided by v_{0M} resulting in prior means for the real and imaginary parts of the coil sensitivities H_{0R} and H_{0I}, respectively

calibration images n_{cal}. The average residual variance over the voxels of the calibration images is calculated to obtain a prior for the noise variance noted as σ_0^2. The hyperparameters α (shape parameter of the inverse gamma) and β (scale parameter of the inverse gamma) are assessed to be $\alpha = n_{cal} - 1$ and $\beta = (n_{cal} - 1)\sigma_0^2$. This prior information is incorporated to reconstruct each voxel measurement in the aliased coil image into the unaliased voxel values at every time in the fMRI series.

The software used for this research was MATLAB run on a 12th Gen Intel(R) Core(TM) i7-1255U laptop computer with 16GB RAM, operating on Windows 11.

4. Simulation and Experimental Studies

Non-Task Data

A noiseless non-task image was used to create two series of 510 simulated full FOV coil images for one slice to mimic the experimental data shown in Subsection 4.6. The last n_{cal} time points of the first time series of non-task images served as calibration images that were utilized for hyperparameter assessment, and the second time series was used for a simulated non-task experiment. A complex-valued image was multiplied by a designed sensitivity map with $n_C = 8$ coils, similar to the four-channel coil shown in Figure 3 but with four additional coils in each corner as well, and then the series of images were Fourier transformed into full coil k-space arrays. In real-world MRI experiments, the first few images of the time series have increased signal as the magnetization reaches a steady state. The first three images in both the simulated series of non-task images are appropriately scaled, based on the experimental data, replicating the increased signal. These series were simulated by adding separate $N(0, 0.0036n_x n_y)$ noise to both time series, where n_y and n_x are the number of rows and columns, respectively, in the full k-space array, to the real and imaginary parts of full coil k-space, corresponding to the noise in the fMRI experimental data used in Section 4. This data generation is following a general linear model with normally distributed noise and no spatial or temporal dependencies.

The arrays were then inverse Fourier transformed back into full coil images. To mimic the fMRI experiment shown in Section 4.6, the first 20 time points were discarded leaving 490 time points of non-task images for the single slice, though they could be used to estimate T_1 and magnetic field maps as described in Section 1.3 of the Supplementary Material. The remaining 490 images in the time series were Fourier transformed and aliased by censoring lines in k-space according to the different acceleration factors used for the simulation, then back transforming the downsampled data.
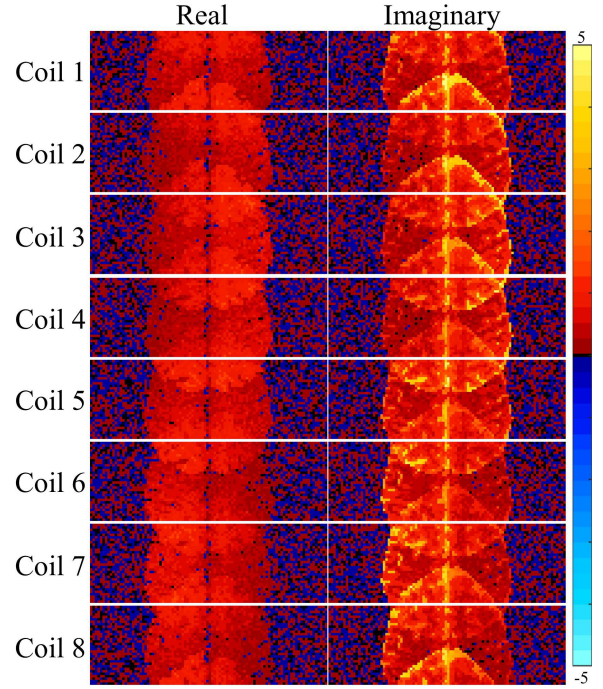

Fig. 8. Simulated observed noisy aliased coil images for first time point in the non-task time series.

Reconstruction Results

To analyze the reconstruction performance of BSENSE vs. SENSE, we first reconstructed aliased coil measurements at one time point, giving us a single unaliased image for both methods. For this, we used the first time point of the 490 simulated non-task time series with an acceleration factor of $n_A = 3$, shown in Figure 8.
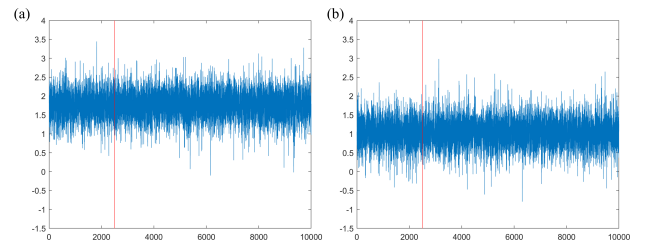

Fig. 9. Time series of the 10,000 iterations from the Gibbs sampler with the real (left) and imaginary (right) components of a gray matter voxel. The red line for both plots indicates the point where the burn-in iterations end.

The last $n_{cal} = 30$ time points, corresponding to 30 seconds, from the first 510 non-task full FOV calibration time series were utilized to assess the hyperparameters. The prior means from the calibration images for the unaliased voxels v_0 and the sensitivity coils S_0 were used as initial values for H and v. These initial values were used to generate a σ^2 value from the posterior conditional from Eq. 2.8, initializing the ICM algorithm and the Gibbs sampler. The simulated aliased coil images were reconstructed into a single, full brain image using the BSENSE MAP estimate from the ICM algorithm, the BSENSE MPM via MCMC, and traditional SENSE estimate. For the ICM algorithm, only three iterations were needed for estimating the parameters (computation time about 0.10 seconds per time point), and for the Gibbs sampling, 10,000 total iterations were run (computation time about 90 seconds per time point) with a burn of 2,500 leaving 7,500 iterations for estimation. Plots of the 10,000 iterations for a gray matter voxel at one single time point is displayed in Figure 9. The plot on the left of Figure 9 is the real part of the complex-valued voxel and the plot on the right is for the imaginary part. The red line in the plots show where the burn-in iterations end. Figure 9 shows that the Gibbs sampler converges relatively quickly. Figure 10 displays the true simulated image (first column) along with the BSENSE MAP unaliased image (second column), the BSENSE posterior marginal mean unaliased image (third column), and the SENSE unaliased image (fourth column).

We can see that the joint MAP estimate and the marginal posterior mean from BSENSE both produce magnitude and phase images that closely resemble the true non-aliased image in Figure 10 (left column). SENSE, on the other hand, produced an image with a higher noise level in the magnitude image resulting in less clear distinction between the different brain tissue when compared to our BSENSE approach and the true unaliased image. This is also evident by examining the noise level outside of the brain which is markedly higher in the

SENSE reconstructed image. Typically, in fMRI studies, the voxels outside the brain are masked out, but here we leave them in to further show the spatial noise level of the reconstructed images for both techniques. Unlike the BSENSE and true phase images, SENSE also produced an unusable phase image with no anatomical structure. Activation using both magnitude and phase images has been shown to yield increased power of detection (Rowe and Logan, 2004; Rowe, 2005) and additional biological information (Petridou et al., 2006).

To quantify the differences between the true and reconstructed magnitude images, we use the mean squared error, $MSE = \frac{1}{K} \sum_{j=1}^{K} (v_j - \overline{v}_j)^2$, where K is the number of voxels (either inside or outside the brain) in the full reconstructed image, v_j is the reconstructed magnitude value of the jth voxel, and $\overline{v}_j$ is the true magnitude value of the jth voxel. This measure will indicate the accuracy of a single reconstructed image compared to the true simulated image with lower MSE indicating a more accurate reconstructed image. The MSE for both BSENSE MAP and BSENSE MPM are <0.001 inside the brain and 0.001 outside the brain, respectively. For SENSE, the MSE was calculated to be 0.035 inside the brain and 0.03 outside the brain. This means that SENSE has a 26,670% larger MSE inside the brain compared to BSENSE MAP and BSENSE MPM, and 2940% and larger MSE outside the brain, respectively. The process illustrated here for reconstructing aliased coil images at a single time point can be replicated to reconstruct the rest of the series.

For the remaining results discussed in this paper, only the BSENSE MAP estimate was used to reconstruct the time series of aliased coil. For the study covered in this paper, we are only interested in a single estimate for each of the reconstructed images. From the Gibbs sampler, that is the posterior mean for each unaliased voxel, v. Since the v follows a normal distribution, the estimated posterior mean and mode would be
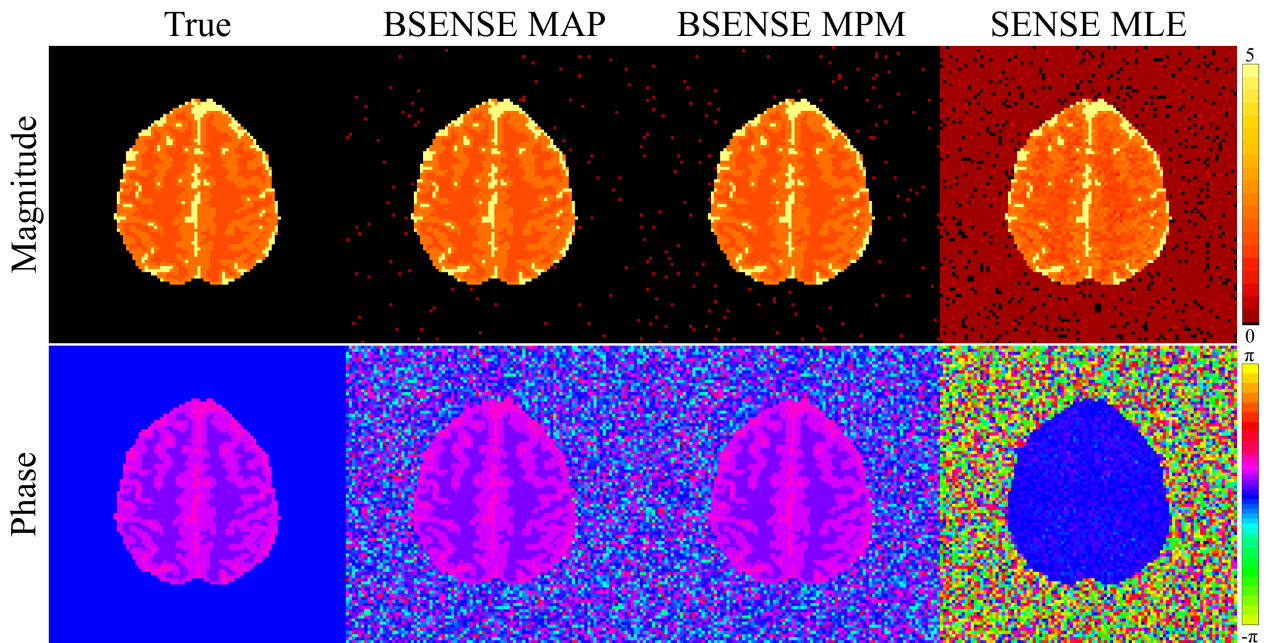

Fig. 10. True non-task unaliased images (first column), BSENSE MAP unaliased non-task images (second column) using ICM, Posterior Mean BSENSE unaliased non-task images (third column) using Gibbs sampling, and SENSE non-task images (fourth column) with magnitude images in the first row and phase images in the second row.

equivalent. This allows us to only need the MAP estimate for image reconstruction for this study, saving computation time.

Next, we evaluated how the number of calibration images, n_{cal}, affected the reconstructed images. For the calibration image analysis, we fixed the acceleration factor to be $n_A = 3$ for the aliased coil measurements of the simulated non-task time series with $n_{TR} = 490$ time points and set the number of calibration images to be $n_{cal} = 5, 10, 15, 20, 25, 30$ for separate hyperparameter assessments. After assessing the hyperparameters using the different numbers of calibration images, the simulated non-task time series with the aliased coil measurements were reconstructed using BSENSE MAP and SENSE.

The results, displayed in Figure 11, indicate that increasing the number of calibration images decreases the noise level outside of the brain for BSENSE but has little effect inside the brain. Even the BSENSE MAP reconstruction with $n_{cal} = 5$ still produces an image with less noise than SENSE. The MSE of inside and outside the brain for both BSENSE and SENSE and the entropy for BSENSE and SENSE for the different number of calibration images were also calculated to quantify this result. Entropy analyzes uncertainty and smoothness across a single image with lower entropy meaning less uncertainty throughout the image. The equation for entropy is given by $E = -\sum_{j=1}^{N}\left[\frac{v_j}{v_{max}}ln\left(\frac{v_j}{v_{max}}\right)\right]$, where ln is the natural log, N is the number of voxels in the full reconstructed image, v_j is the reconstructed magnitude value of the jth voxel, and v_{max} is the voxel intensity if all the image intensities were in one pixel given by $v_{max} = \sqrt{\sum_{j=1}^{N} v_j{}^2}$ (Atkinson et al., 1997).
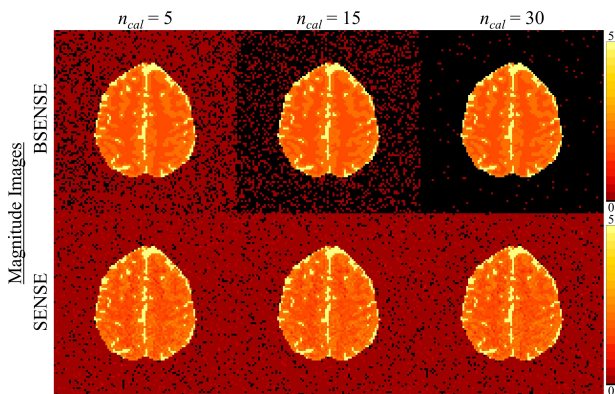
Fig. 11. Reconstructed magnitude images for different number of calibration images using BSENSE MAP estimate (top row) and SENSE (second row).

Shown in Figure 12a, the MSE for inside and outside the brain for the BSENSE MAP reconstructed magnitude images was immensely smaller than the SENSE reconstructed magnitude images. BSENSE also had much smaller entropy compared to SENSE, displayed in Figure 12b, as it decreased from 193.6 to 181.4 with the entropy for SENSE remaining around 218.5 as the number of calibration images increased. Lower MSE for BSENSE indicates a more precise reconstructed image while smaller entropy means less uncertainty with image reconstruction. Increasing the number of calibration images also decreases the temporal variance for BSENSE yielding increased SNR. For SENSE, the number of calibration images does not meaningfully affect the temporal variance, resulting in similar SNR for each n_{cal}. In all cases, the

temporal variance for BSENSE is substantially lower than for SENSE. This demonstrates that BSENSE mitigates noise in the reconstructed image.
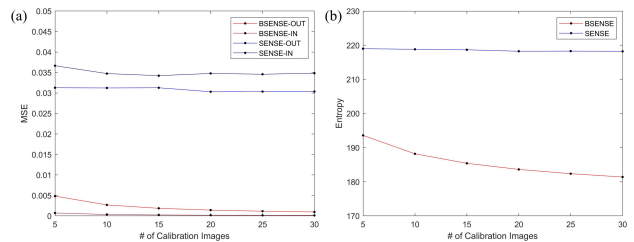
Fig. 12. (a) MSE for inside and outside the brain for BSENSE and SENSE comparing both method's reconstructed images to the true simulated magnitude image for each number of calibration images. For the MSE plot, BSENSE is shown in red for outside the brain (blue for SENSE) and dark red for inside the brain (dark blue for SENSE). (b) Entropy plot for BSENSE and SENSE for each number of calibration images where BSENSE is shown red, and SENSE is shown in blue.

Along with analysis of the number of calibration images, we evaluated how different acceleration factors, n_A, affected the reconstructed images. Here, we fixed the number of calibration images to be $n_{cal} = 30$ for hyperparameter assessment and set the acceleration factors of the non-task time series to be $n_A = 2, 3, 4, 6, 8, 12$. For SENSE, the maximum acceleration factor was $n_A = 8$ since it cannot exceed the number of coils used as it yields a severely under-determined system of equations. These aliased coil measurements with separate acceleration factors were reconstructed into full images using the BSENSE MAP estimate and SENSE, again comparing the results for both methods.

The results, exhibited in Figure 13, showed that the reconstructed magnitude images from BSENSE are negligibly affected by increasing the acceleration factor with SENSE being severely affected. The reconstructed phase images for BSENSE applying the different acceleration factors also closely resemble the true phase image while the reconstructed phase images for SENSE show zero phase inside the brain, rendering unusable phase information for anatomical and task analysis. These phase results are shown in Section 1.1 of the Supplementary Material. The BSENSE temporal variance stays relatively the same (first row of Figure 14) with the increased acceleration
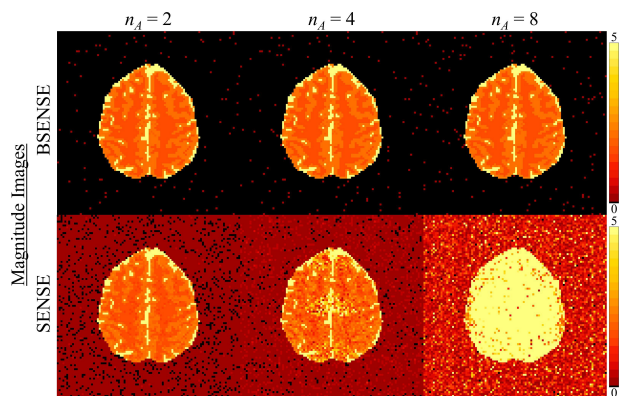
Fig. 13. Reconstructed magnitude images for different acceleration factors using BSENSE MAP estimate (top row) and SENSE (second row).

factors, still producing high SNR (third row of Figure 14). SENSE was heavily influenced by the acceleration factor, as the reconstructed images with acceleration factors greater than $n_A = 3$ fail to produce usable images with distinct matter types throughout the brain as shown in Figure 13. The increased acceleration factor also markedly increases the temporal variance (second row of Figure 14) which substantially degrades the SNR of SENSE (fourth row of Figure 14).
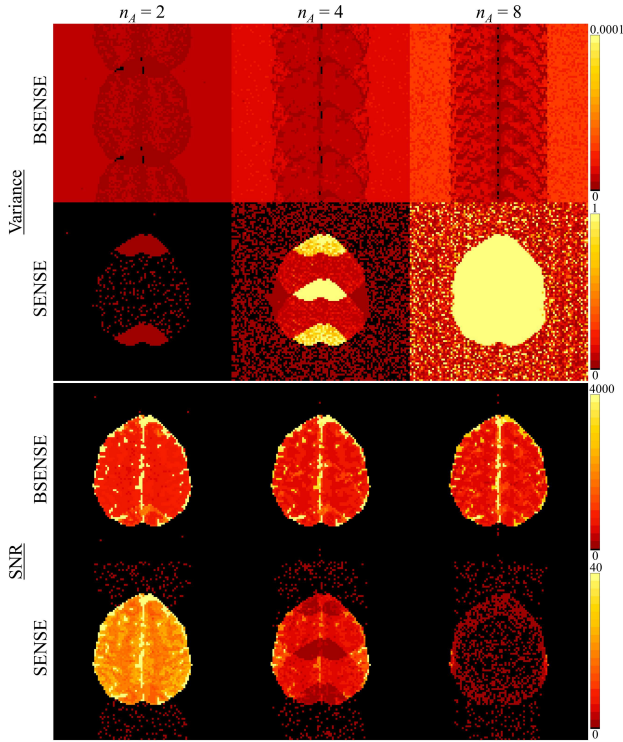

Fig. 14. Temporal variance and SNR images for different acceleration factors using BSENSE MAP estimate (first row and third row, respectively) and SENSE (second row and fourth row, respectively).

We examined the reconstruction time of both methods for the different acceleration factors as well. The average time, in seconds, it took to reconstruct each image in the time series for BSENSE decreased from 0.1195 seconds to 0.0744 moving from an acceleration factor of 2 to 8 with a slight increase to 0.0855 with an acceleration factor of 12. SENSE does have a shorter reconstruction time with it decreasing from 0.0441 seconds to 0.0201 moving from an acceleration factor of 2 to 8. Despite this, our BSENSE approach still offers the potential for real time image reconstruction while producing remarkably better results in image reconstruction.

Task Activation

In task-based fMRI, the non-task reconstructed images create a baseline value for each voxel giving us an intercept only simple linear regression $y = \beta_0 + \varepsilon$ where y is the unaliased voxel value. By adding in task activation to select images in the series of images, we have a simple linear regression $y = \beta_0 + x\beta_1 + \varepsilon$ for the unaliased voxel values. In this regression, β_0 is the baseline voxel value from the non-task reconstructed images determining the SNR $= \beta_0/\sigma$, and β_1 is the estimated task related increase from β_0 determining the contrast-to-noise ratio

CNR $= \beta_1/\sigma$. The vector $x \in \{0,1\}^{n_{IMG}}$, where n_{IMG} is the number of reconstructed images in the series, is a vector such that the zeros correspond to the images in the series without task activation and ones corresponding to the images with task activation. We can write this regression as $y = XB + \varepsilon$, where $X = [1, \quad x] \in \mathbb{R}^{n_{IMG} \times 2}$ and $B = [\beta_0, \beta_1]'$.

Since the CNR is typically much lower than the SNR, the task is not usually visible on the reconstructed images. Instead, a right-tailed t-test is carried out with $\beta_1 \leq 0$ as the null hypothesis and $\beta_1 > 0$ as the alternative. The reason for the one-sided hypothesis test is because we anticipate an increased signal from the task activation. To simulate added task, a $\beta_1 = 0.045$ magnitude-only signal increase is added to the true noiseless non-task image with $\varepsilon \sim N(0, 0.0036)$ noise yielding a CNR of 0.75. A simulated phase task of $\pi/120$ was also added and analyzed in Section 1.3 of the Supplementary Material. This added task activation is located in the left motor cortex to resemble the region of interest (ROI) of brain activity from the fMRI unilateral right-hand finger tapping experiment (Karaman, Bruce, and Rowe, 2014). Ranges of tissue pixel intensities are $1.00 - 1.75$ for white matter, $1.75 - 3.00$ for grey matter, and $4.00 - 6.00$ for the cerebral spinal fluid (CSF) in the simulation to mimic the experimental data discussed in Subsection 4.6.

FMRI Time Series Data Generation

A true noiseless task image along with a true noiseless non-task image were used to simulate a series of 510 full FOV coil images for one slice. The true images were multiplied by the same $n_C = 8$ coil sensitivity maps used for the non-task simulated time series, and then the series of images were Fourier transformed in full coil k-space arrays. This series was also generated by adding separate $N(0, 0.0036n_x n_y)$ noise to the real and imaginary parts of the full coil k-space arrays and were then inverse Fourier transformed back into full coil images. To simulate the real-world fMRI experimental process, the series was generated by starting with 20 non-task time points. The scaling for the first few images in the fMRI simulated data was the same as the signal increases outlined in Subsection 4.1 for each of the tissue types. The initial 20 non-task time points are followed by 16 epochs alternating between 15 non-task and 15 task time points. An epoch is a stimulation period with time points of the subject at rest (non-task) and the subject performing an action or task. The series culminated with 10 non-task time points producing the simulated fMRI series of 510 images. To mimic the forthcoming fMRI experiment, the first 20 time points were discarded leaving 490 time points in the series. The last n_{cal} time points in the non-task time series from Subsection 4.1 were utilized as full FOV coil calibration images to assess the hyperparameters. For this simulation, we evaluate both BSENSE and SENSE using $n_C = 5, 10, 15, 20, 25, 30$ calibration images. The transformation and aliasing are the same as in Subsection 4.1. The different acceleration factors tested in this simulated fMRI experiment are $n_A = 2, 3, 4$.

FMRI Time Series Reconstruction Results

The hypothesis test described in Subsection 4.3 was utilized to determine voxels with a statistically significant signal increase. The statistically significant voxels for each number of calibration images were analyzed for the BSENSE MAP reconstructed time series and the SENSE reconstructed time series using the 5% false discovery rate (FDR) threshold procedure (Benjamini and Hochberg, 1995; Genovese, Lazar,
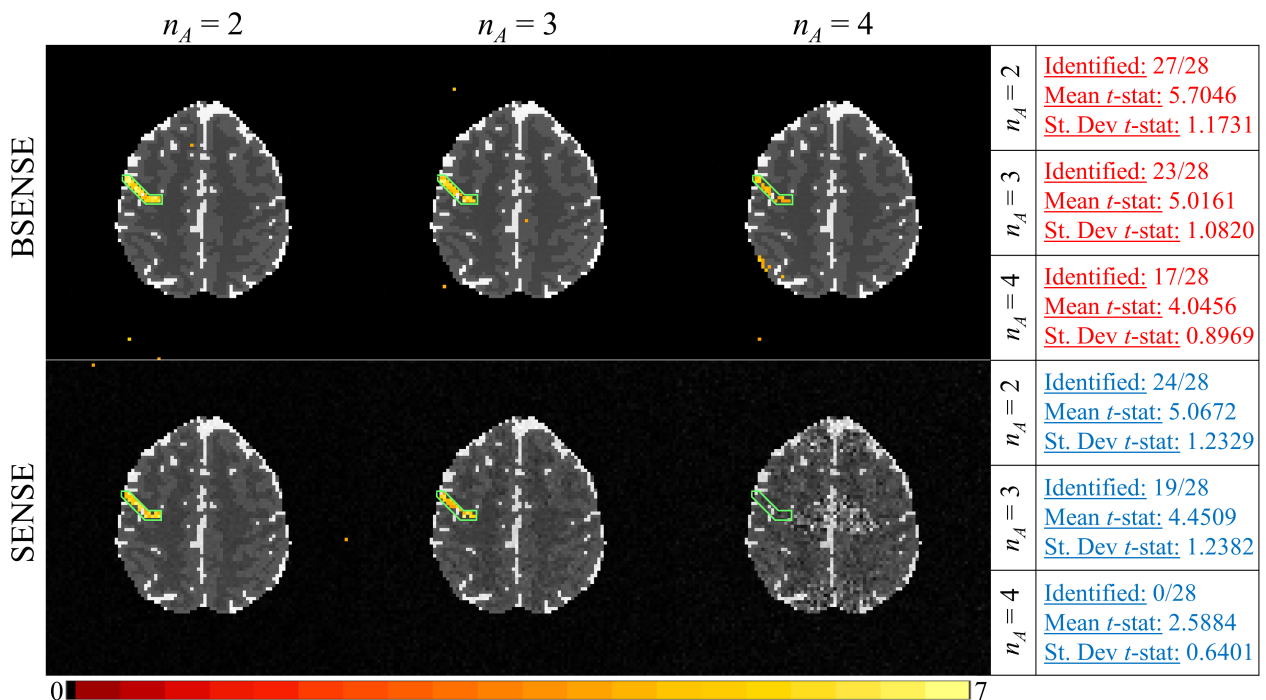
Fig. 15. Statistically significant voxels in the ROI using FDR for BSENSE reconstructed images (first row), significant voxels in the ROI using FDR for SENSE (second row), and analysis of the t-statistics in the boxes on the right with BSENSE in red and SENSE in blue.

and Nichols, 2002; Logan and Rowe, 2004). The ROI here consists of 28 voxels located in the left motor cortex. Increasing the number of calibration images did not notably affect the detection of task for either BSENSE or SENSE, shown in Section 1.3 of the Supplementary Material. The number of identified voxels with task activation and the mean value of the t-statistics was greater with BSENSE while having a smaller standard deviation compared to SENSE. These results indicate our BSENSE approach performs better with task detection compared to traditional SENSE, regardless of the number of calibration images that are utilized for hyperparameter assessment.

Figure 15 shows the statistically significant magnitude-only voxels from the BSENSE MAP reconstructed time series (first row) and the SENSE reconstructed time series (second row) for the different acceleration factors. Figure 15 also summarizes the t-statistics in the ROI for each acceleration factor. BSENSE identified more statistically significant voxels in the ROI for each acceleration factor while SENSE does not detect a single voxel when the acceleration factor was $n_A = 4$. The mean value for the t-statistics was again much higher for BSENSE with a lower standard deviation for the different acceleration factors compared to SENSE, demonstrating that BSENSE performs better when detecting task activation. Increasing the acceleration factor decreases the number of voxels identified and the mean of the t-statistics for both BSENSE and SENSE. The false positive rate for BSENSE for each of the acceleration factors were 0.033%, 0.033%, and 0.098%, respectively, while SENSE had 0.022%, 0%, and 0%, respectively.

Experimental Data Description

A 3.0 T General Electric Signa LX magnetic resonance imager was used to conduct an fMRI experiment on a single subject. The last $n_{cal} = 30$ full k-space arrays of a non-task series of 510 time points performed on the subject was inverse Fourier transformed into full coil brain images and used for hyperparameter assessment. A bilateral finger-tapping task was performed in a block design with an initial 20 s rest followed by 16 epochs with 15 s off and 15 s on. The experiment was concluded with 10 s of rest giving us a series of $n_{IMG} = 510$ repetitions with each repetition being 1 s, a flip angle of 90° and an acquisition bandwidth of 125 kHz. The data set consists of nine 2.5 mm thick axial slices with $n_C = 8$ receiver coils that have a 96×96 dimension for a 24 cm full FOV, with a posterior to anterior phase encoding direction. For this paper, the time series for all nine slices was used to analyze the effects of applying acceleration factors of $n_A = 2, 3, 4$ for both BSENSE and SENSE, but only the time series of the second slice is shown. Like the simulation study, the aliased coil images came from artificially skipping lines in the full coil k-space arrays, mimicking the effect of actually subsampling the coil k-space arrays. The first 20 images were discarded due to varying echo times and magnetization stability, leaving 490 time points for the fMRI experiment. The first 10 images not used for fMRI activation can be used to estimate a T_1 map (Karaman et al., 2014) as shown in Section 2.2 of the Supplementary Material while the second 10 images could be used for static magnetic field mapping (Hahn, Nencka, and Rowe, 2012), also discussed in the Supplementary Material.

Before artificially aliasing the time series by omitting lines of k-space, a reference image (left image in Figure 16) was produced by taking the square norm between the $n_C = 8$ full FOV coil images at the first time point. This provides a magnitude image with which to compare to SENSE and our BSENSE. Rows of k-space in the fMRI experiment were omitted in each coil in accordance to the specified acceleration factors.
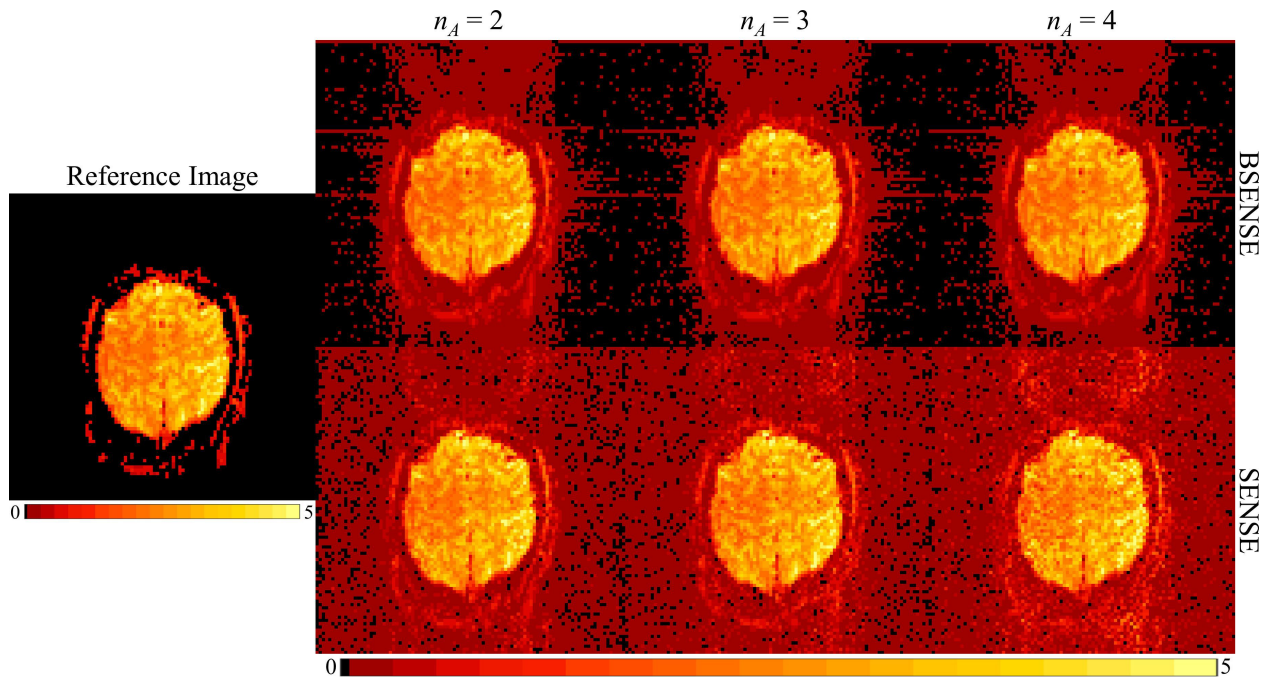
Fig. 16. BSENSE MAP unaliased non-task magnitude images for each acceleration factor (first row) using the ICM algorithm, and SENSE unaliased non-task magnitude images for each acceleration factor (second row) with the magnitude reference image (left).

Experimental Results

Similar to the process for the simulated data described in Section 4, each image in the entire time series of aliased coil measurements were simultaneously unaliased and combined using BSENSE and SENSE separately. Figure 16 displays the

BSENSE MAP reconstructed images (top row) and the SENSE reconstructed images (bottom row) of the first time point of the 490 images using acceleration factors 2, 3, and 4. Just as the simulated results in Figure 13 demonstrated, the BSENSE reconstruction in Figure 16 produced clearer, less noisy images
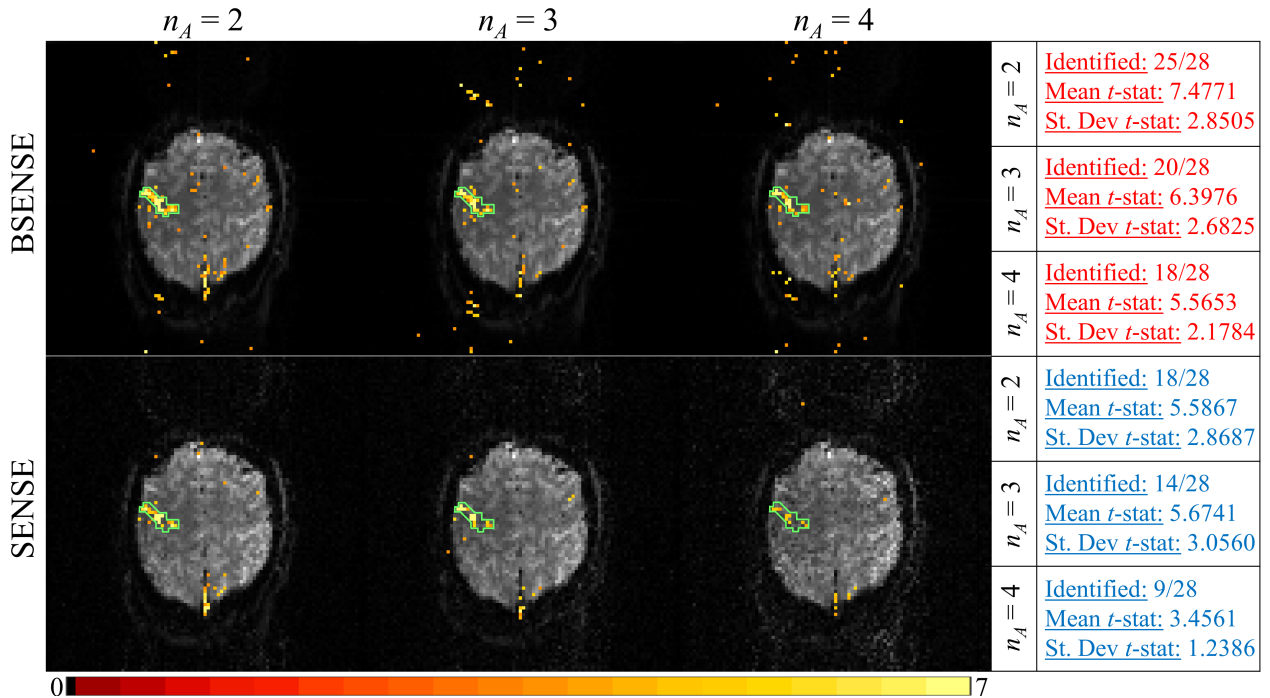

Fig. 17. Statistically significant voxels in the ROI using FDR for BSENSE reconstructed images (first row) for three different acceleration factors, significant voxels in the ROI using FDR for SENSE (second row) for three different acceleration factors, and analysis of the t-statistics to the right of the images with BSENSE in red and SENSE in blue.

compared to SENSE reconstruction. It is noticeable inside of the brain where the signal is higher, but the distinction is strongest outside the brain.

MSE was again utilized to quantify the differences between the reference image and reconstructed images. The MSE for inside the brain for the BSENSE MAP was approximately 0.016 for each acceleration factor. For SENSE, the MSEs inside the brain were 0.030, 0.038, and 0.170 for acceleration factors 2, 3, 4, respectively. The MSE for outside the brain for BSENSE was 0.034, 0.033, and 0.033 for each of the acceleration factors while the MSE for SENSE was 0.061, 0.085, and 0.157. This means SENSE had an 88%, 140%, and 968% larger MSE inside the brain and an 81%, 160%, and 379% larger MSE outside the brain, respectively, for each acceleration factor. These results reflect the decreased noise from BSENSE versus SENSE. The entropy for BSENSE (191.0, 190.2, and 190.2, respectively) was also lower than the entropy for SENSE (214.9, 226.6, 243.3) indicating less uncertainty for each reconstructed image.

For the detection of task activation, the hypothesis test outlined in Subsection 4.3 was carried out. Figure 17 shows the statistically significant voxels under BSENSE (top row) and SENSE (bottom row) reconstruction. The images for the statistically significant voxels in Figure 17 for both methods use the 5% FDR threshold. Voxels outside the brain are usually masked out meaning the statistically significant voxels shown outside the brain in Figure 17 would typically not be there. Figure 17 also summarizes the t-statistics with BSENSE (red) and SENSE (blue). BSENSE correctly detected more voxels than SENSE as task activation in the ROI for all three acceleration factors. Our BSENSE approach also had a much higher mean t-statistic and lower standard deviation for all the acceleration factors. The false positive rate for BSENSE for each of the acceleration factors were 0.697%, 0.664%, and 0.642%, respectively, while SENSE had 0.283%, 0.163%, and 0.109%, respectively. We also evaluated BSENSE and SENSE task detection performance on the other eight slices which is outlined in Section 2.2 of the Supplementary Material.

5. Discussion

In linear regression, having an unknown design matrix and complex-valued parameters can make parameter estimation of the regression coefficients more difficult. Here, we implement a Bayesian complex-valued latent variable linear model and applied it, along with the non-Bayesian model, to image reconstruction in fMRI. The results of the simulated and experimental studies showed that the Bayesian complex-valued latent variable model (BSENSE) out performed the complex-valued model (SENSE).

The BSENSE unaliased images were shown to more accurately reconstruct the truth compared to SENSE. The number of calibration images had minimal effect on the SENSE reconstructed images and its performance against BSENSE reconstructed images. Increasing the number of calibration images, however, did reduce the noise level in the BSENSE reconstructed images, leading to increased SNR. The results also indicated that the different acceleration factors had less influence on BSENSE than SENSE. BSENSE was able to successfully reconstruct images with an acceleration factor of up to 12, which was greater than the $n_C = 8$ coils used, without any aliasing artifacts or increasing the spatial variance but diminished activation. The SENSE reconstructed images beyond acceleration factors of $n_A = 3$ were essentially unusable.

Our BSENSE approach also had better performance when detecting the signal increase in the voxels that experienced task activation, as shown with both simulated and experimental data. The number of coils did not have a notable effect on our BSENSE approach which indicates that it works for any coil configuration as demonstrated in Section 1.1 of the Supplementary Material. There was a noticeable effect on the SENSE image reconstruction. With four coils, the noise for the SENSE reconstructed images was higher compared to the 8, 12, and 16 simulated coil arrays as shown in Section 1.1 of the Supplementary Material. This suggests that SENSE requires a deeper coil sensitivity map coverage to properly reconstruct images.

This paper used the full posterior distribution for reconstructing images, meaning available prior information was quantified on all three parameters (v, S, and σ^2) and utilized for parameter estimation. We have also analytically integrated out σ^2 yielding a marginal posterior where v and S are the only two unknowns to be estimated. Integrating out σ^2 produces a joint Student-t posterior for S and v from which we have obtained Gibbs sampling marginal estimates consistent with the three-parameter model.

For the task detection in this paper, only the MAP estimate using the ICM algorithm was used to reconstruct the time series of non-task and task aliased images for capturing activation for both the simulated and experimental data. This is due to the Gibbs sampler being more computationally expensive when running a long series of images so it may not be as practical to use compared to evaluating the MAP estimate. This does not mean there is no value in running a Gibbs sampler, as it has the additional benefit of quantifying uncertainty. For instance, it could be utilized on a shorter series of images, provide us more statistical information about any voxel, or for hypothesis testing between two images. It is also possible to hybridize the ICM and Gibbs sampler with a couple of ICM steps followed by a short or no-burn Gibbs sampler. Our Bayesian approach allows for more options of how to run an fMRI experiment based on the objective of the scan compared to SENSE.

In this paper, a magnitude-only activation model was utilized to detect task activation. In Section 1.3, phase-only activation for BSENSE is analyzed with the results showing strong task detection power. Since the reconstructed images are complex-valued, our model is expected to be applicable for complex activation models for task detection (Rowe and Logan, 2004; Rowe, 2005). Further, an extension of our model would be to incorporate both covariance between the observations and covariance between the regression coefficients.

References

Atkinson, D., Hill, D. L. G., Stoyle, P. N. R., Summers, P. E., and Keevil, S. F. (1997). Automatic correction of motion

artifacts in Magentic Resonance images using an entropy focus criterion. *IEEE Transactions on Medical Imaging* **16,** 903–910.

Bandettini, P., Jesmanowicz, A., Wong, E., and Hyde, J. S. (1993). Processing strategies for time-course data sets in functional MRI of the human brain. *Magnetic Resonance in Medicine* **30,** 161–173.

Benjamini, Y. and Hochberg, Y. (1995). Controlling the false discovery rate: a practical and powerful approach to multiple testing. *Journal of the Royal Statistical Society, Series B* **57,** 289–300.

Bruce, I. P., Karaman, M. M., and Rowe, D. B. (2012). The SENSE-Isomorphism Theoretical Image Voxel Estimation (SENSE-ITIVE) model for reconstruction and observing statistical properties of reconstruction operators. *Journal of Magnetic Resonance Imaging* **30,** 1143–1166.

Chen, S. H., Lee, Y. S., and Wang, J. C. (2018a). Complex-valued Gaussian process latent variable model for phase-incorporating speech enhancement. *IEEE International Conference on Acoustics, Speech and Signal Processing* pages 5439–5443.

Chen, S. H., Lee, Y. S., and Wang, J. C. (2018b). Locality preserving discriminative complex-valued latent variable model. *24th International Conference on Pattern Recognition* pages 1169–1174.

Gelfand, A. E. and Smith, A. F. M. (1990). Sampling-based approaches to calculating marginal mensities. *Journal of American Statistical Association* **85,** 398–409.

Geman, S. and Geman, D. (1984). Stochastic relaxation, Gibbs distributions, and the Bayesian restoration of images. *IEEE Transactions on Pattern Analysis and Machine Intelligence* **6,** 721–741.

Genovese, C. R., Lazar, N. A., and Nichols, T. E. (2002). Thresholding of statistical maps in functional neuroimaging using the false discovery rate. *Neuroimage* **15,** 870–878.

Hahn, A. D., Nencka, A. S., and Rowe, D. B. (2012). Enhancing the utility of complex-valued functional magnetic imaging detection of neurobiological processes through postacquisition estimation and correction of dynamic B_0 errors and motion. *Human Brain Mapping* **33,** 288–306.

Hoerl, A. E. and Kennard, R. W. (1970). Ridge regression: biased estimation for nonorthogonal problems. *Technometrics* **12,** 55–67.

Karaman, M. M., Bruce, I. P., and Rowe, D. B. (2014). A statistical fMRI model for differential T_2* contrast incorporating T_1 and T_2* of gray matter. *Journal of Magnetic Resonance Imaging* **32,** 9–27.

King, K. F. and Angelos, L. (2001). SENSE image quality improvement using matrix regularization. *Proceedings of the 9th Annual Meeting of ISMRM* page 1771.

Kumar, A., Welti, D., and Ernst, R. R. (1975). NMR Fourier zeugmatography. *Journal of Magnetic Resonance Imaging* **18,** 69–83.

Liang, Z. P., Bammer, R., Ji, J., Pelc, N. J., and Glover, G. H. (2002). Making better SENSE: wavelet denoising, Tikhonov regularization, and total least squares. *Proceedings of the 10th Annual Meeting of ISMRM* page 2388.

Lin, F. H., Kwong, K. K., Belliveau, J. W., and Wald, L. L. (2004). Parallel imaging reconstruction using automatic regularization. *Magnetic Resonance in Medicine* **51,** 559–567.

Lindley, D. V. and Smith, A. F. M. (1972). Bayes estimates for the linear model. *Journal of the Royal Statistical Society, Series B* **34,** 1–18.

Liu, B., King, K., Steckner, M., Xie, J., Sheng, J., and Ying, L. (2009). Regularized sensitivity encoding (SENSE) reconstruction using Bregman iterations. *Magnetic Resonance in Medicine* **61,** 145–152.

Logan, B. R. and Rowe, D. B. (2004). An evaluation of thresholding techniques in fMRI analysis. *Neuroimage* **22,** 95–108.

Loizou, P. C. (2013). *Speech Enhancement*. CRC Press.

Nguyen, A. H. T., Reju, V. G., Khong, A. W. H., and Soon, I. Y. (2017). Learning complex-valued latent filters with absolute cosine similarity. *IEEE International Conference on Acoustics, Speech and Signal Processing* pages 2412–2416.

Ogawa, S., Lee, T. M., Nayak, A. S., and Glynn, P. (1990). Oxygenation-sensitive contrast in magnetic resonance image of rodent brain at high magnetic fields. *Magnetic Resonance in Medicine* **14,** 68–78.

O'Hagan, A. (1994). *Kendall's Advanced Theory of Statistics, vol. 2B*. Wiley, New York.

Petridou, N., Dietmar, P., Silva, A. C., Loew, M., Bodurka, J., and Bandettini, P. A. (2006). Direct magnetic resonance detection of neuronal electrical activity. *Proceedings of the National Academy of Sciences* **103,** 16015–16020.

Pruessmann, K. P., Weiger, M., Scheidegger, M. B., and Boesiger, P. (1999). SENSE: sensitivity encoding for fast MRI. *Magnetic Resonance in Medicine* **42,** 952–962.

Rowe, D. B. (2005). Modeling both the magnitude and phase of complex-valued fMRI data. *Neuroimage* **25,** 1310–1324.

Rowe, D. B. and Logan, B. R. (2004). A complex way to compute fMRI activation. *Neuroimage* **23,** 1078–1092.

Schreier, P. J. and Schraf, L. L. (2010). *Statisical signal processing of complex-valued data: the theory of improper and noncircular signals*. Cambridge University Press.

Tibshirani, R. (1996). Regression shrinkage and selection via the lasso. *Journal of the Royal Statistical Society, Series B* **58,** 267–288.

Williamson, D. S., Wang, Y., and Wang, D. (2013). A sparse representation approach for perceptual quality improvement of separated speech. *IEEE International Conference on Acoustics, Speech and Signal Processing* pages 7015–7019.

Williamson, D. S., Wang, Y., and Wang, D. (2014). A two-stage approach for improving the perceptual quality improvement of separated speech. *IEEE International Conference on Acoustics, Speech and Signal Processing* pages 7034–7038.

Ying, L., Xu, D., and Liang, Z. P. (2004). On Tikhonov regularization for image reconstruction in parallel MRI. *26th Annual International Conference of the IEEE Engineering in Medicine and Biology Society* pages 1056–1059.

PAPER

A Bayesian Complex-Valued Latent Variable Model Applied to FMRI Supplementary Material

Chase J. Sakitis,[1] D. Andrew Brown[2] and Daniel B. Rowe[1,*]

[1]Mathematical and Statistical Sciences, Marquette University, 1313 W. Wisconsin Ave., 53233, WI, USA and [2]Mathematical and Statistical Sciences, Clemson University, 220 Pkwy Dr., 29634, SC, USA
*Corresponding author. daniel.rowe@marquette.edu

Abstract

In linear regression, the coefficients are simple to estimate using the least squares method with a known design matrix for the observed measurements. However, real-world applications may encounter complications such as an unknown design matrix and complex-valued parameters. The design matrix can be estimated from prior information, but can potentially cause an inverse problem when multiplying by the transpose as it is generally ill-conditioned. This can be combat by adding regularizers to the model, but does not always mitigate the issues. Here, we propose our Bayesian approach to a complex-valued latent variable linear model with an application to fMRI image reconstruction. The complex-valued linear model and our Bayesian model evaluated through extensive simulations and applied to experimental fMRI data.

Simulation Results

Non-Task Reconstruction

As mentioned in Section 4.1 of the main paper, the first few images in an fMRI time series have increased signal as the magnetization reaches a stable state. To mimic this, the first three of the 510 time points of the simulated non-task time series were scaled with the signal slightly decreasing from the first to the third time point before reaching a stable signal in the fourth time point. The scaling was determined by dividing the first three images by the 21st time point, separately. After dividing the three images, the signal increase for each tissue type (white matter, grey matter and CSF) was averaged together for each of the three divided images, calculating the average signal increase for each matter type. For example, the average signal increase in the first image for the white matter was 40%, 55% for the grey matter and 75% for the CSF giving multiplication factors of 1.40, 1.55, and 1.75 for the matter types, respectively. This process was repeated for the second and third image in the series with the multiplication factors decreasing from the first to the third image. The first 10 time points of an fMRI experiment can be used to estimate a T_1 map which efficiently segments the different tissue types, which is demonstrated later in this Supplementary Material. The next 10 time points can be utilized to estimate a magnetic field map to adjust for geometric distortions (Karaman et al., 2015). These first 20 time points are typically discarded in the task detection component of fMRI analysis.

Since the reconstructed images are complex-valued, we are able to examine the phase images. The phase of the reconstructed images for a different number of calibration images is shown in Figure 1 for BSENSE (top row) and SENSE

(bottom row). The images in Figure 1 indicate that increasing the number of calibration images has little to no effect on the phase of the reconstructed images for both BSENSE and SENSE. Similar to the phase images displayed in Section 4.2 of the main paper, the SENSE phase images show no anatomical structure while the BSENSE phase images resemble the true simulated phase.
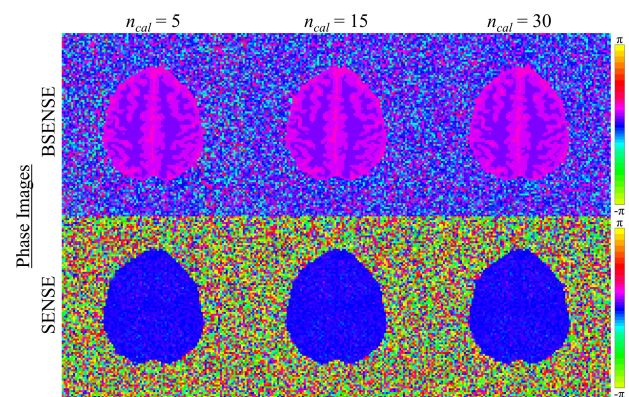

Fig. 1. Phase of the reconstructed images for different number of calibration images using BSENSE MAP estimate (top row) and SENSE (bottom row).

Along with analyzing different number of calibration images, we also examined phase images for different acceleration factors. Figure 2 displays the phase of reconstructed images for both BSENSE (top row) and SENSE (bottom row) using
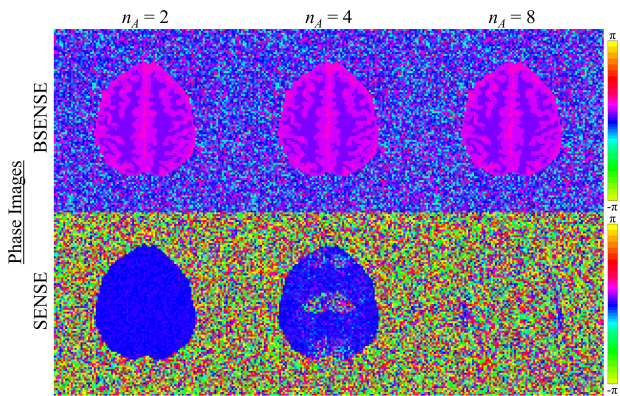
Fig. 2. Reconstructed phase images for different acceleration factors using BSENSE MAP estimate (top row) and SENSE (bottom row).

Fig. 4. Plot for the average correlation between all voxels and the voxels they were previously aliased with for each subsampling size of the calibration images. The red line indicates subsampling without replacement and the blue line indicates subsampling with replacement for both plots.

acceleration factors of 2, 4, and 8. The phase images for BSENSE are unaffected by the different acceleration factors. For SENSE, the phase images appear to be overtaken by noise as the acceleration factor increases.

For the simulated and experimental data, $n_C = 8$ coils were used to evaluate the reconstruction results for BSENSE and SENSE. We also wanted to test how different coil configurations would affect the image reconstruction results for the BSENSE and SENSE magnitude images. Figure 3 shows that the MSE for the magnitude BSENSE MAP reconstructed images are smaller than the magnitude SENSE reconstructed images when compared to the true simulated image for each number of coils. Also, SENSE had a noticeably higher MSE for $n_C = 4$ coils in the configuration compared to $n_C = 8, 12, 16$. This indicates that SENSE requires coils with higher coverage of the field-of-view while BSENSE still produces highly accurate reconstructed images.

For estimating priors of BSENSE, we use up to 30 calibration image time points which are averaged together and then utilized to assess the hyperparameters. This means
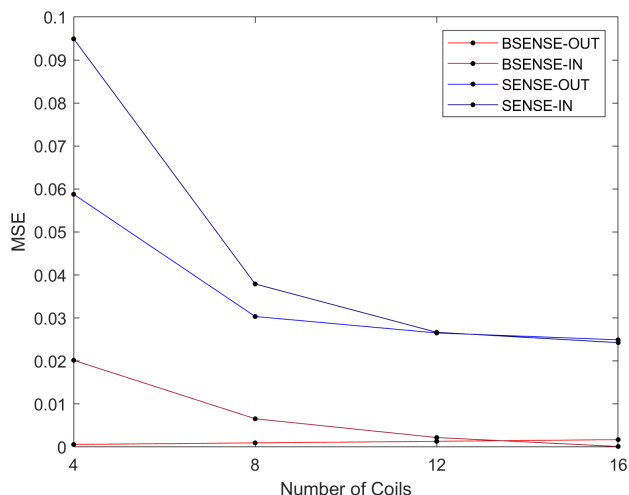
the same prior information is used at each time point when reconstructing the fMRI time series which could potentially lead to correlation with previously aliased voxels or task leakage. Task leakage is false detection of task in voxels that were previously aliased. To possibly mitigate this, we can randomly subsample (with or without replacement) the calibration images used at each time point in the fMRI time series. This means different hyperparameters are applied at each time point to the reconstruction of the aliased time series. We can also change the prior scalars n_v and n_S in the parameter estimation equations 3.6, 3.7, and 3.8 to be less than the number the calibration which decreases the weight of the prior information in the reconstructed images.

Figure 4 demonstrates the effects of subsampling the calibration images on magnitude voxel correlation while decreasing the prior scalars to $n_v = 1$ and $n_S = 1$. Figure 4 shows a plot of the average correlation between all voxels and the voxels they were previously aliased with for subsampling sizes of 5, 10, 15, 20, 25, and 27, out of 30 calibration images, comparing them to the non-subsampling BSENSE that has been demonstrated throughout the main paper. The results indicate that subsampling the calibration images, either with or without replacement, remarkably decrease the correlation between voxels and their previously aliased voxels.

Coil Sensitivity and Residual Noise

Along with the unaliased voxel values, BSENSE estimated the coil sensitivities for each TR in the time series. Figure 5a displays the true magnitude image (center) and the true magnitude coil sensitivities starting with coil 1 on the top middle and going clockwise to coil 8. Figure 5b has the same setup with the BSENSE magnitude reconstructed image and coil sensitivities for the first TR of the 490 non-task time series. The estimated BSENSE coil sensitivities appear to be similar to the the true coil sensitivities.

The estimated coil sensitivities were also analyzed using different number of calibration images (5, 10, 15, 20, 25, 30) and acceleration factors (2, 3, 4, 6, 8, 12). With fixing

Fig. 3. MSE for inside and outside the brain for BSENSE and SENSE comparing both method's magnitude reconstructed images to the true simulated magnitude image for each number of coils (4, 8, 12, 16). BSENSE is shown in red for outside the brain (blue for SENSE) and dark red for inside the brain (dark blue for SENSE).
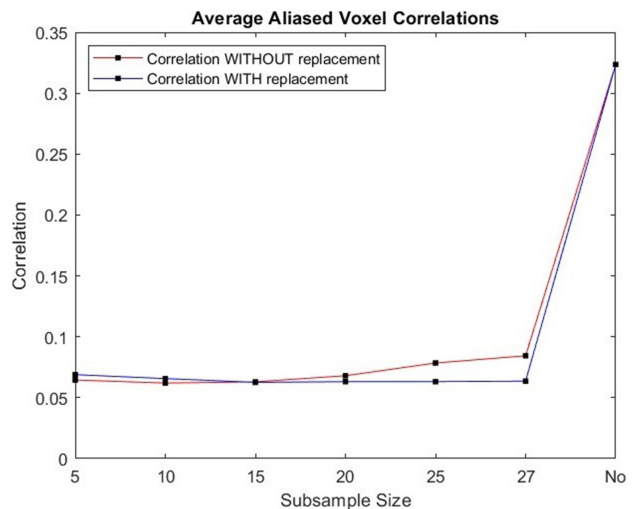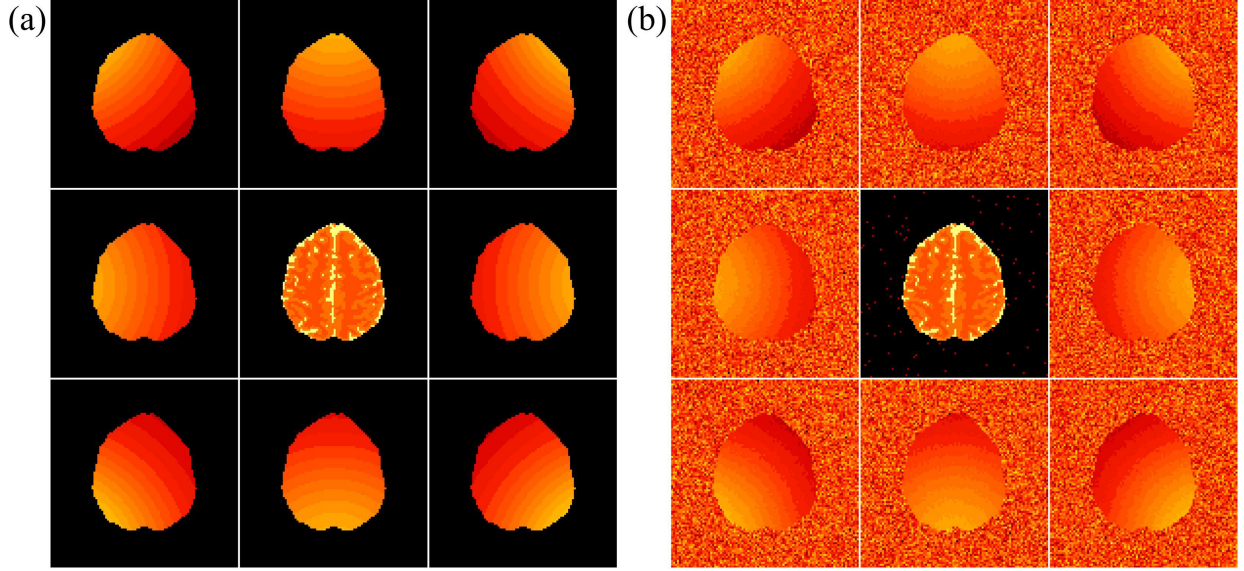
Fig. 5. (a) True magnitude coil sensitivities surrounding the true magnitude image and (b) BSENSE estimated magnitude coil sensitivities surrounding the reconstructed magnitude image.

$n_A = 3$, Figure 6a exhibits the MSE for the different number of calibration images for each coil inside the brain. The MSE for each coil is very small and decreases as the number of calibration images increase, similar to the MSE decreasing outside the brain in the BSENSE magnitude reconstructed images. With fixing $n_{cal} = 30$, Figure 6b exhibits the MSE for the different acceleration factors for each coil inside the brain. Again, the MSE for each coil is very small with a slight increase as the acceleration factor increases. This illustrates that our BSENSE approach accurately estimates the simulated coil sensitivities as well.

Our proposed BSENSE technique also estimated the residual variance for the aliased coil measurements. We evaluated the affects of the number of calibration images and acceleration factors on the residual variances. Figure 7a shows the residual variances of the coil measurements for each

number of calibration images with $n_A = 3$. The residual variance appears to increase as the number of calibration images increase. This is due to the coefficients for the estimation of σ^2, outlined in Subsection 3.3 of the main paper, increasing with the number of calibration images. Figure 7b shows the residual variances of the coil measurements for each acceleration factor with $n_{cal} = 30$. The residual variance appears to decrease as the acceleration factor increases because the denominator of the Iterated Conditional Modes (ICM) estimate of σ^2 is increasing. All residual variances appear to be uniform across the aliased images in Figure 7 which is expected as noise is anticipated to be uniform across the image.
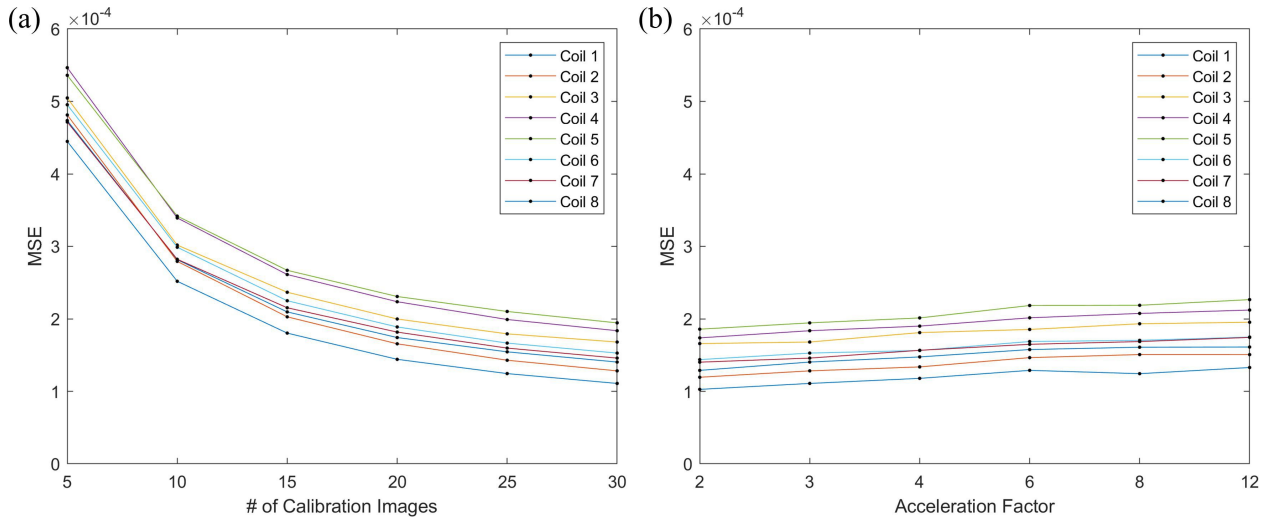

Fig. 6. (a) MSE for each of the $n_C = 8$ coils using a different number of calibration images and (b) MSE for each of the $n_C = 8$ coils using different acceleration factors.
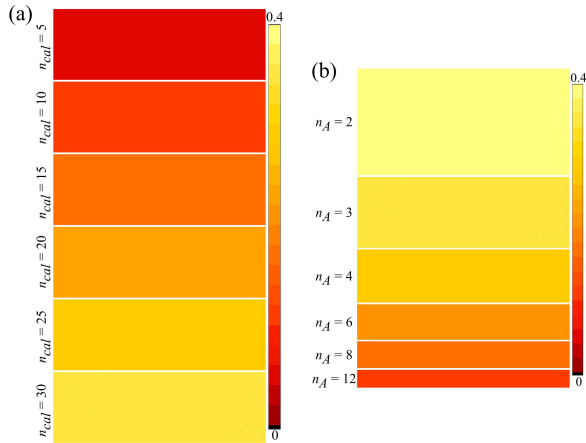
Fig. 7. (a) Residual variance of the aliased coil images for each number of calibration images and (b) Residual variance of the aliased coil images for each acceleration factor.

Fig. 8. Estimated T_1 map from the ratio of the first time point image over the time points 6-10 where the magnetization reaches stability in the simulated data. The scale is from zero seconds to two seconds, equivalently 2000 ms.

Simulated fMRI

As mentioned above, the first 10 time points in an fMRI experiment can be used to estimate a T_1 map of the brain. To reconstruct the first image of the simulated fMRI time series, the first time point of the non-task time series was utilized as a calibration image to assess hyperparameter of the first time point. The same was accomplished for the second and third points as well since they also experiencing increased but declining signals. The rest of the time points from the 20 that were discarded in the fMRI experiment were reconstructed using the priors from the hyperparameter assessment that used the last 30 time points from the non-task simulated time series. Before estimating the T_1 map, we first calculated $R = M_1/M_{SS}$ where M_1 is the magnitude of the reconstructed first time point and M_{SS} is the average magnitude images of time points six through 10 (Karaman, Bruce, and Rowe, 2015). Then the T_1 map was estimated by $T_1 = \frac{TR}{ln[R/(R-1)]}$ where TR is the repetition time, which is 1 s for our data, and ln is the natural log (Karaman, Bruce, and Rowe, 2015). Figure 8 displays the estimated T_1 map for the simulated fMRI time series. The values estimated for the grey matter and the white in the T_1 map for the simulated data were approximately 1410 ms and 1199 ms, respectively. These values are consistent with those found in literature where, using a 3 Tesla machine, of 1331 ms for grey matter and 832 ms for white matter as shown by Karaman, Bruce, and Rowe, 2015. These results show that BSENSE preserves quantitative T_1 estimation and considering the accurate reconstructed phase images, should be able estimate the change in the B-field inhomogeneity, ΔB.

Similar to magnitude-only task detection, we can also use the phase images for task detection. As mentioned in the Section 4.3 of the main paper, a simulated phase task of $\pi/120$ was added to the simulated true simulated task image. A simple linear regression model, $\phi = \theta_0 + \theta_1 x + \eta$, can be used for the phase activation as well. In this regression, ϕ is the phase of the unaliased voxel, θ_0 is the baseline phase voxel value from the non-task reconstructed images, θ_1 is the estimated increase from θ_0, and $x \in \{0,1\}^{n_{IMG}}$ is a vector such that the zeros correspond to the images in the series without task activation and ones corresponding to the images with task activation. We then use a one-tailed t-test, $t = \hat{\theta}_1/SE(\hat{\theta}_1)$,
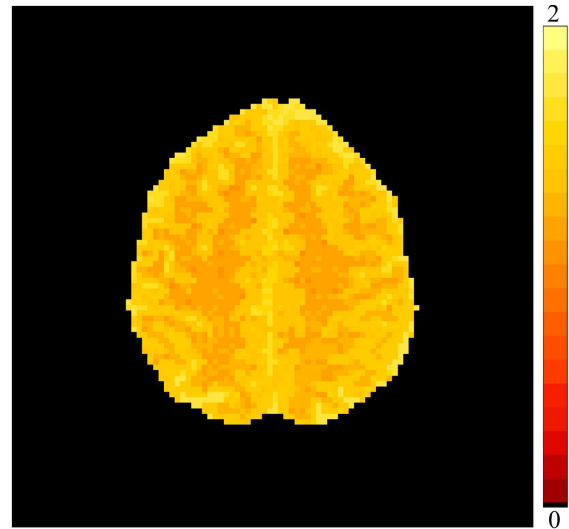
to determine which voxels contain statistically significant θ_1 values indicating which voxels experience task activation.
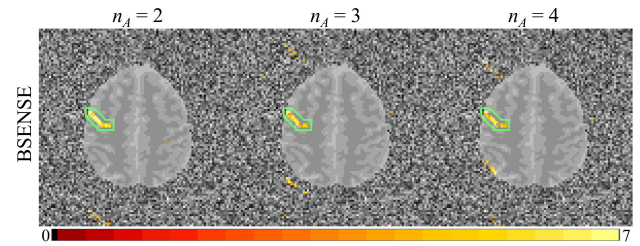

Fig. 9. Statistically significant voxels in the ROI using FDR for different acceleration factors from the BSENSE phase reconstructed images.

Using the 5% FDR threshold, Figure 9 shows phase activation for BSENSE reconstructed time series using acceleration factors of 2, 3, and 4. Like the BSENSE reconstructed magnitude images, we can see that it captures the simulated task activation in the ROI. Since the phase images for SENSE are unusable without any anatomical structure, it is unreasonable to analyze phase task activation.

In Section 1.1 of the Supplementary Material, we examined how subsampling from 30 calibration images for hyperparameter assessment at each time point effects correlation with other voxels. Here, we analyzed how the same subsampling parameters effect task detection for BSENSE fixing the prior scalars $n_v = 1$ and $n_S = 1$. Figure 10a displays the number of voxels identified as task in the ROI along with the top and bottom task leakage from unaliasing. Figure 10b illustrates the mean of the t-values in the ROI, the voxels in the top leakage, and the voxels in the bottom leakage. For both plots in Figure 10, the red lines and blue lines indicate subsampling with and without replacement, respectively, the lines with black dots are the values for the ROI, the lines with the dark grey dots are the values for the top leakage region, and
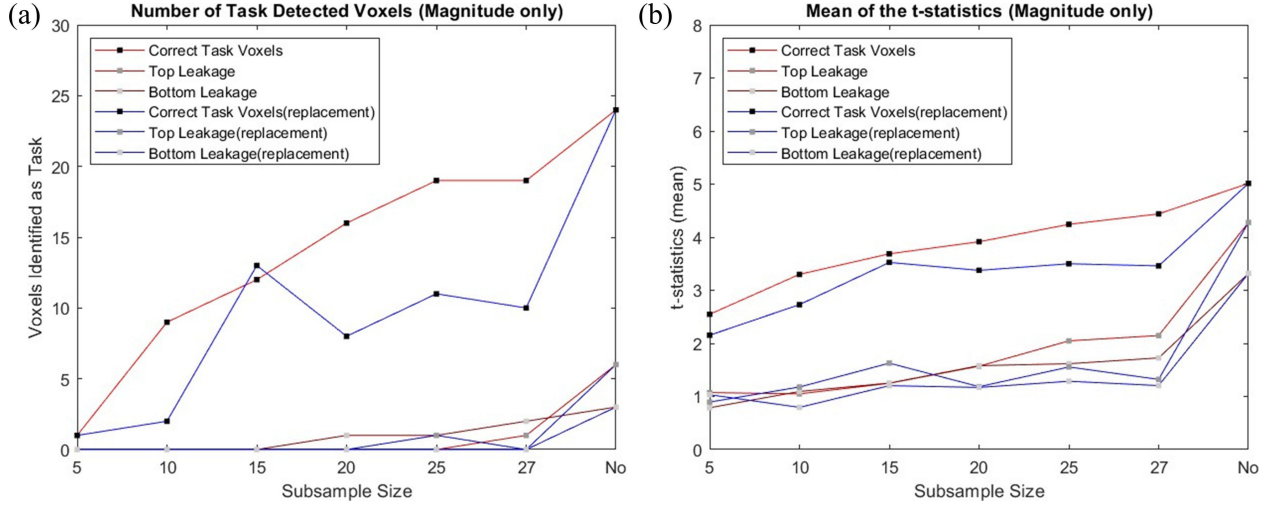
Fig. 10. (a) Plot for number of voxels detected as task activation in the ROI and location of the potential task leakage (with $n_A = 3$) for each subsample size for bootstrapping the calibration image. (b) Plot for mean of the t-statistics of voxels in the ROI and location of the potential task leakage (with $n_A = 3$) for each subsample size for bootstrapping the calibration images. The red lines indicate subsampling without replacement and the blue lines indicate with replacement. The lines with the black dots indicate the lines for analysis inside the ROI, The dark grey dot lines indicate analysis for the top task leakage, and the light grey dot lines for analysis of the bottom task leakage.

the lines with the light grey dots are the values for the bottom leakage region.

As demonstrated in Figure 10a, the number of task voxels correctly identified slightly decreases when introducing subsampling and subsample size decreases. Except for 15, subsampling without replacement does correctly identify more task voxels than with replacement. Subsampling the calibration images does decrease the number of voxels incorrectly identified as task in the leakage areas. Corresponding results for this method is exhibited in analyzing the mean t-statistics shown in Figure 10. Introducing subsampling does decrease the mean of the t-values compared to the normal BSENSE method, but also decreases the t-values' mean in the areas of leakage as well. Subsampling without replacement has higher average t-values than with replacement and both decrease as the subsample size decreases as well. These task detection results coincide with the correlation results of subsampling which ultimately decrease correlation and task leakage but also decrease the power of task detection in the ROI.
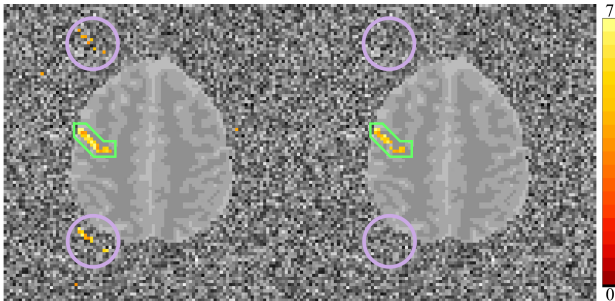

Fig. 11. Task detection from the phase reconstructed images using an acceleration of 3 for normal BSENSE (left) and subsampling of 27 calibration images without replacement with prior scalars of $n_v = 1$ and $n_S = 1$ from Eqs. 3.6, 3.7, and 3.8 (right).

With the simulated fMRI series using an acceleration factor of $n_A = 3$, we examined the effect subsampling would have on phase task detection. Figure 11 displays the images of phase task activation using normal BSENSE (left) and subsampling BSENSE of size 27 without replacement and prior scalars of $n_v = 1$ and $n_S = 1$ (right) with purple circles showing the locations of potential task leakage. It appears that subsampling removes the task leakage that normal BSENSE experiences, but slightly decreases the number of active voxels in the ROI.

Real-World Experimental Data

Data Description

Additional details of the experimental data are described in this subsection. For each volume image in the experimental series, a time dependent echo time, TE_t, consisted of three parts. The first part was fixed to have a value of $TE = 42.7$ ms at the first 10 time points. In the second part, the next five TE values were an equally spaced interval of values 42.7 ms, 45.2 ms, 47.7 ms, 50.2 ms, and 52.7 ms and was repeated for another 5 time points. For the final part, the last 490 time points were fixed at 42.7 ms. To account for T_1 effects and varying echo times, the center row of k-space for each TR in each receiver coil was acquired with three navigator echoes which is used to correct any potential Nyquist "ghosting." The additional rows of k-space were integrated to estimate and adjust the error in the center frequency and group delay offsets between the odd and even lines of k-space (Nencka, Hahn, and Rowe, 2008).

Typically, the magnetic fields in an fMRI experiment will induce a drift in the phase over time which we correct before reconstruction to give us a stable phase through time. First, the angular phase temporal mean of the time-series is calculated and subtracted for each voxel time-series. A local second order polynomial was spatially fit to the resultant difference of the voxel phase time-series. Then the fitted polynomial is added to the mean phase image producing a steady phase over time for each coil.

Experimental Data Results

The BSENSE and SENSE reconstruction results for the experimental data, outlined in Subsection 5.1 of the main paper, are further demonstrated in this section. Similar to the simulated fMRI experiment, the first and six through 10 time points of the 20 discard time points in the experimental data were utilized to estimate a T_1 map as shown in Figure 12. For the grey and white matters, the T_1 estimation values were approximately 1410 ms and 1267ms, respectively, which closely resembles the T_1 estimates from the simulation study and those found in the literature.
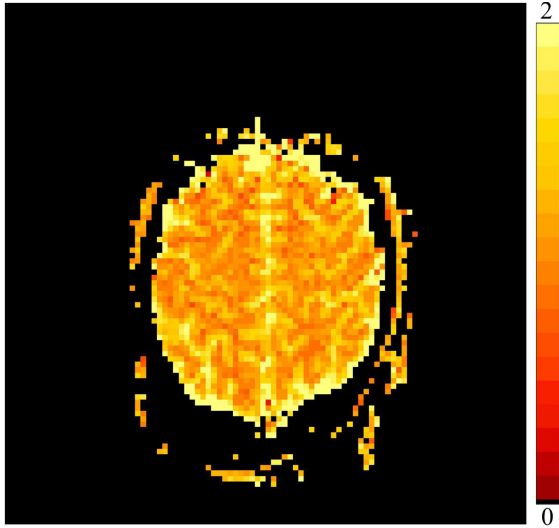

Fig. 12. Estimated T_1 map from the ratio of the first time point image over the time points 6-10 where the magnetization reaches stability in the experimental data. The scale is from zero seconds to two seconds, equivalently 2000 ms.

Figure 13 displays the time series of two reconstructed voxels using BSENSE (red) and SENSE (blue): one voxel not in the ROI (non-task) and one voxel in the ROI (task). These plots show much smaller temporal variability with BSENSE.

We also analyzed the phase of the reconstructed experimental time series using acceleration factors of $n_A = 2, 3, 4$, displayed in Figure 14. The appearance of the BSENSE phase reconstructed images are due to the imperfect shims of the magnetic field gradients. An example of this can be seen in the experimental data of the Bruce et al. 2011 paper. In the simulated data used for the this study, perfect homogeneity throughout the magnetic gradient field is assumed resulting in clear anatomical structure for the BSENSE phase
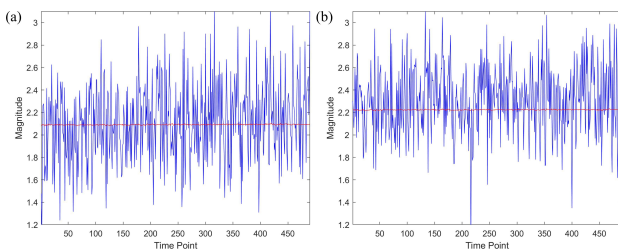

Fig. 13. (a) Time series of a non-task voxel and (b) Time series of a task voxel.

reconstructed images in Figure 8 of the main paper. The BSENSE reconstructed phase images in Figure 14 more accurately represent the phase images and can also be utilized estimate the change in the B-field inhomogeneity, ΔB. Like the magnitude images, increasing the acceleration factor has little effect of the BSENSE reconstructed phase images, but appear to cause the SENSE reconstructed phase images to be noisier.
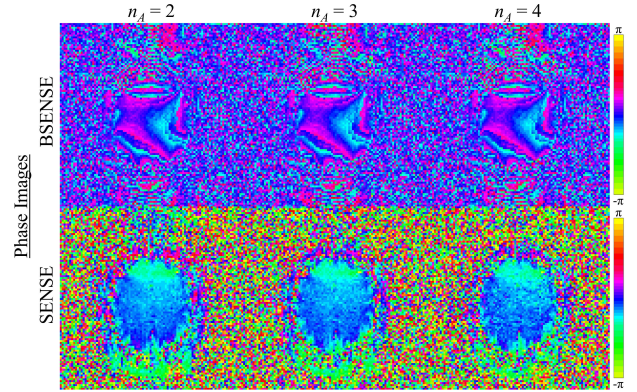

Fig. 14. Reconstructed phase images for different acceleration factors using BSENSE MAP estimate (top row) and SENSE (bottom row) from the experimental data.

We evaluated BSENSE and SENSE task detection performance on all nine slices utilizing 30 calibration images and applying an acceleration factor of 3. Both methods were visually compared to the reference task detection image for each slice. For each slice of experimental data, we estimated single magnitude images at each time point by taking the root sum of squares of the full coil images. The series of the magnitude images was then utilized to estimate task activation using the same linear regression described in Section 4.3 of the main paper to yield the reference task detection images. Figure 15 shows the statistically significant voxels for the root sum of squares of the full coil images (left column), the BSENSE MAP estimate (middle column) and the SENSE (right column) reconstructed experimental time series for each slice. For the The images for the statistically significant voxels in Figure 15 for each techniques use the 5% FDR threshold. For this real-world fMRI experiment, only slices 1-4 observe task activation in our ROI which is the left motor cortex. Figure 15 also displays the analysis of the t-statistics for each slice with activation for both BSENSE (red) and SENSE (blue). Note that BSENSE correctly identified more voxels than SENSE as task activation in the ROI for all four slices. The BSENSE technique also had a higher mean t-statistic for each slice, and the standard deviation is lower for all but one of the slices (fourth slice). These experimental results demonstrate that our proposed BSENSE technique performs better with detecting activation compared to SENSE for multiple slices.

Further Discussion

The main paper described theoretical advantages of BSENSE image reconstruction over SENSE image reconstruction. It also exhibited statistical improvements of BSENSE over SENSE through simulated and experimental applications. These applied results mainly focused on magnitude reconstructed images, temporal variance, SNR, and magnitude-only task
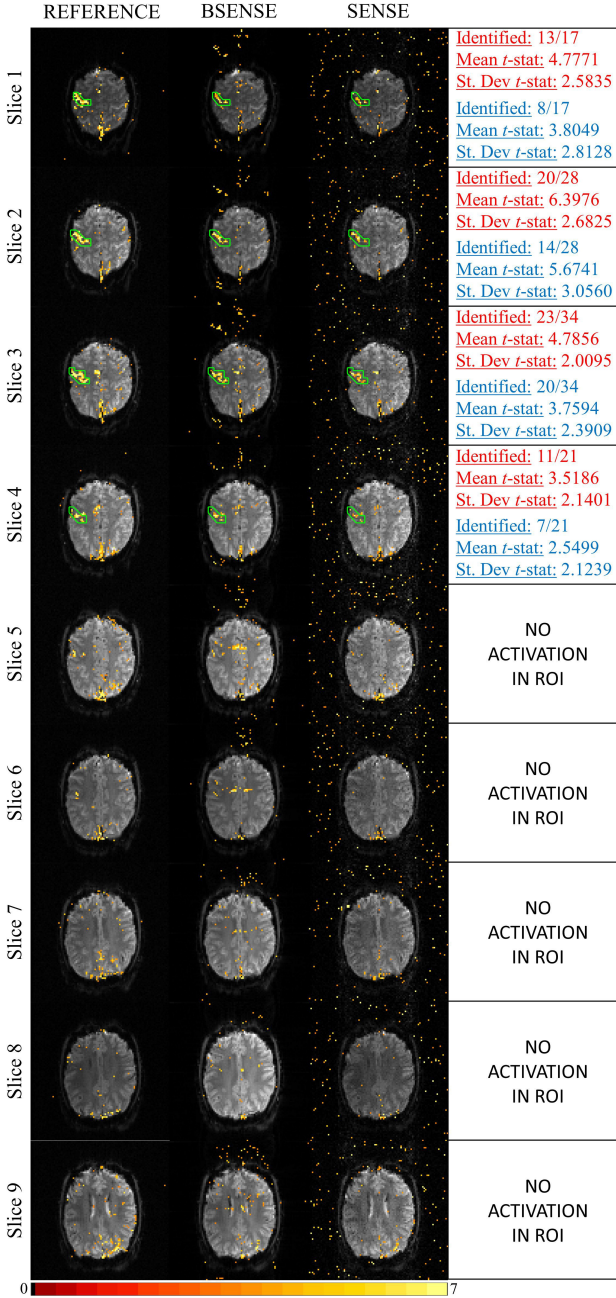
Fig. 15. Statistically significant voxels in the ROI using FDR for root sum of squares of the full coil images (left column), statistically significant voxels in the ROI using FDR for BSENSE reconstructed images (middle column), significant voxels in the ROI using FDR for SENSE (right column), and analysis of the t-statistics in the boxes on the right with BSENSE in red and SENSE in blue.

detection. This Supplementary Material further supported the improved results by looking at the phase of the reconstructed images for both simulated and real-world experimental data and analyzing phase activation with the simulated data.

Beyond the reconstructed images, BSENSE also successfully estimated the sensitivities of the coils and uniformity of the noise variance of the aliased coil images. We were also able to successfully estimate a T_1 map for both simulated and experimental data. Our BSENSE model, and the SENSE

model, assume there is no correlation between the previously aliased voxels (Bruce, Karaman, and Rowe, 2012) along with no correlation between the coils when reconstructing the aliased coil measurements. The correlation between previously aliased voxels was addressed, without changing the model, by performing the subsampling of the calibration images. This method decreased the effects of unaliasing by decreasing the correlation of the previously aliased voxels along with decreasing the leakage in detecting task activation. These improvements from subsampling make it reasonable to apply this method over normal BSENSE to MR image reconstruction. This enhances the flexibility of our BSENSE technique which increases its practical use for real-world fMRI experiments.

Appendix: Table of Variables

n_C	Number of coils
n_A	Acceleration factor
a_C	Observed complex-valued aliased coil voxel measurements
a_R	Real component of the observed complex-valued aliased coil voxel measurements
a	Real-valued representation of the observed complex-valued aliased coil measurements
a_I	Imaginary component of the observed complex-valued aliased coil voxel measurements
S_C	Unobserved complex-valued coil sensitivities
S_R	Real component of the unobserved complex-valued coil sensitivities
S_I	Imaginary component of the unobserved complex-valued coil sensitivities
S	Real-valued isomorphic representation of the unobserved complex-valued coil sensitivities
v_C	Unobserved complex-valued unaliased voxel values
v_R	Real component of the unobserved complex-valued unaliased voxel values
v_I	Imaginary component of the unobserved complex-valued unaliased voxel values
v	Real-valued representation of the unobserved complex-valued unaliased voxel values
ε_C	Additive image space measurement error
ε_R	Real component of the additive image space measurement error
ε_I	Imaginary component of the additive image space measurement error
σ^2	Variance of the additive image space measurement error
H	Representation of the real and imaginary components of the sensitivity coils not in isomorphic form
v_0	Complex-valued prior mean for the unaliased voxels, v, in the BSENSE model in real-valued representation
v_{0M}	Magnitude of the prior mean for the unaliased voxels, v, in the BSENSE model
n^v	Scalar prior for the unaliased voxels, v, in the BSENSE model
H_0	Complex-valued prior mean for the coil sensitiviites, S, in the BSENSE model in real-valued representation

S_0	Complex-valued prior mean for the coil sensitiviites, S, in the BSENSE model in real-valued skew symmetric representation
n^S	Scalar prior for the coil sensitiviites, S, in the BSENSE model
α	Shape parameter for the inverse gamma distribution of σ^2 in the BSENSE model
β	Scale parameter for the inverse gamma distribution of σ^2 in the BSENSE model
Y	Real-valued representation of a_c where the real component is stacked in the first column and the imaginary component is stacked in the second column
V	Transpose of the skew symmetric matrix representation of v_c
n_Y	Number of rows in the full k-space array
n_X	Number of columns in the full k-space array
n_{cal}	Number of calibration time points used for hyperparameter assessment
v_j	Magnitude of the jth voxel in the reconstructed image
$\overline{v}_j$	Magnitude of the jth voxel in the true simulated image
v_j	The magnitude voxel intensity if all image intensities were in one voxel
y	The reconstructed voxel for the task detection linear regression model
X	The design matrix for the task detection linear regression model
B	The coefficients for the task detection linear regression model
n_{IMG}	The number of images in an fMRI time series

References

Bruce, I. P., Karaman, M. M., and Rowe, D. B. (2011). A statistical examination of SENSE image reconstruction via an isomorphism representation. *Journal of Magnetic Resonance Imaging* **29,** 1267–1287.

Bruce, I. P., Karaman, M. M., and Rowe, D. B. (2012). The SENSE-Isomorphism Theoretical Image Voxel Estimation (SENSE-ITIVE) model for reconstruction and observing statistical properties of reconstruction operators. *Journal of Magnetic Resonance Imaging* **30,** 1143–1166.

Karaman, M. M., Bruce, I. P., and Rowe, D. B. (2015). Incorporating relaxivities to more accurately reconstruct MR images. *Journal of Magnetic Resonance Imaging* **33,** 374–384.

Nencka, A. S., Hahn, A. D., and Rowe, D. B. (2008). The use of three navigator echos in Cartesian EPI reconstruction reduces Nyquist ghosting. *Proceedings of the 16th Annual Meeting of ISMRM* **3032,**.